NASA TECHNICAL NOTE

NASA TN D-6140

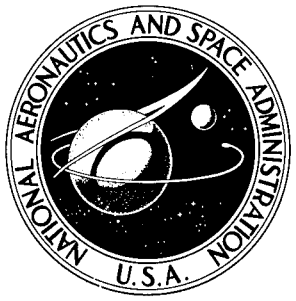

NASA TN D-6140

TORSIONAL SHEAR STRENGTH OF FILAMENT-WOUND GLASS-EPOXY TUBES

by L. David Wall, Jr., and Michael F. Card

Langley Research Center
Hampton, Va. 23365

NATIONAL AERONAUTICS AND SPACE ADMINISTRATION • WASHINGTON, D. C. • AUGUST 1971

1. Report No. NASA TN D-6140	2. Government Accession No.	3. Recipient's Catalog No.
4. Title and Subtitle TORSIONAL SHEAR STRENGTH OF FILAMENT-WOUND GLASS-EPOXY TUBES		5. Report Date August 1971 6. Performing Organization Code
7. Author(s) L. David Wall, Jr., and Michael F. Card		8. Performing Organization Report No. L-7058 10. Work Unit No. 134-14-01-02
9. Performing Organization Name and Address NASA Langley Research Center Hampton, Va. 23365		11. Contract or Grant No. 13. Type of Report and Period Covered Technical Note
12. Sponsoring Agency Name and Address National Aeronautics and Space Administration Washington, D.C. 20546		14. Sponsoring Agency Code
15. Supplementary Notes		

16. Abstract

Results are presented from torsion tests conducted on 36 multilayered, filament-wound, glass-epoxy tubes. Configurations with helical windings and with alternating helical and circumferential windings were investigated for various winding angles. Under small loadings, shear moduli deduced from linear shear stress-strain curves were found to be in reasonable agreement with analytical predictions. Under larger loadings, various degrees of nonlinearity in shear stress-strain curves were encountered, depending on the helical winding angle. Experimental torsional strengths were defined by a 0.2-percent offset yield stress or by maximum stress when large nonlinearities did not exist. These strengths were compared with torsional buckling predictions for orthotropic cylinders, and with material strength predictions based on orthotropic yield criteria and elastic stress analysis. Computed elastic buckling stresses were considerably higher than the experimental strengths for most of the test specimens except for those with only 30° and 45° windings. Experimental torsional strengths were found to correlate with conventional yield predictions if predicted yielding in certain layers were ignored or if unrealistically large transverse tensile and shear strengths of unidirectional laminae were employed in the analysis.

17. Key Words (Suggested by Author(s)) Composite material Shear strength Torsional buckling	18. Distribution Statement Unclassified – Unlimited		
19. Security Classif. (of this report) Unclassified	20. Security Classif. (of this page) Unclassified	21. No. of Pages 46	22. Price* $3.00

*For sale by the National Technical Information Service, Springfield, Virginia 22151

TORSIONAL SHEAR STRENGTH OF FILAMENT-WOUND GLASS-EPOXY TUBES

By L. David Wall, Jr., and Michael F. Card
Langley Research Center

SUMMARY

Results are presented from torsion tests conducted on 36 multilayered, filament-wound, glass-epoxy tubes. Configurations with helical windings and with alternating helical and circumferential windings were investigated for various winding angles. Under small loadings, shear moduli deduced from linear shear stress-strain curves were found to be in reasonable agreement with analytical predictions. Under larger loadings, various degrees of nonlinearity in shear stress-strain curves were encountered, depending on the helical winding angle. Experimental torsional strengths were defined by a 0.2-percent offset yield stress or by maximum stress when large nonlinearities did not exist. These strengths were compared with torsional buckling predictions for orthotropic cylinders and with material strength predictions based on orthotropic yield criteria and elastic stress analysis. Computed elastic buckling stresses were considerably higher than the experimental strengths for most of the test specimens except for those with only 30° and 45° windings. Experimental torsional strengths were found to correlate with conventional yield predictions if predicted yielding in certain layers were ignored, or if unrealistically large transverse tensile and shear strengths of unidirectional laminae were employed in the analysis.

INTRODUCTION

The development of high-performance glass, boron, and carbon filaments has resulted in many studies of the application of fiber-reinforced structures to aerospace structures. Successful design with such structures requires a thorough knowledge of the strength of fibrous composites for a wide variety of configurations under tensile, compressive, and shear loads. Although some experimental information is available on the strength of fibrous composites, there is no substantial body of reliable data available for shear loadings.

In the experimental determination of the shear strength of a multilayered composite, a variety of test methods including beam, plate, and tube tests can be employed. The circular tube or cylindrical shell is considered to be the most reliable specimen for

measurement of shear strength since torsional loadings produce the most easily understood state of stress in the test section. Unfortunately, test programs on the torsional shear strength of tubular specimens have been generally limited to a few isolated tests. Available test data for glass- and boron-reinforced tubes or cylindrical shells are given in references 1 to 7.

The purpose of the present paper is to report the results of an experimental investigation of the torsional strength and stiffness of 36 glass-epoxy multilayered filament-wound tubes. Two basic winding configurations were studied: one with helical windings, the other with alternating helical and circumferential windings. Torsional stiffnesses and strengths of tubes with various helical winding angles were determined experimentally. Shear moduli are compared with analytical estimates. Shear strengths based on ultimate or yield stress are compared with predictions from orthotropic buckling theory and with orthotropic yield criteria using the methods summarized in reference 8. The experimental program described herein has been complemented by a similar program (unpublished) in which the axial compressive strength of glass-epoxy tubes was investigated.

SYMBOLS

Measurements and calculations were made in U.S. Customary Units. The values for the physical quantities are given both in the International System of Units (SI) and in U.S. Customary Units. A table of conversion factors is given in appendix A. The relationship between these two systems of units can be found in reference 9.

a,b constants associated with orthotropic yield criteria (eq. (5))

B_{ij} elastic constants in inverted form of strain-stress relations (B3)

C_{ij} extensional stiffness of cylinder wall

D_{ij} bending stiffness of cylinder wall

E Young's modulus

E_L,E_T Young's modulus of unidirectional layer in direction parallel and perpendicular to fibers, respectively

E_x,E_y Young's moduli for layer associated with cylinder surface coordinates

$\overline{E}_x$ effective axial modulus of cylinder wall

G	shear modulus
G_{LT}	shear modulus of unidirectional layer
G_{xy}	shear modulus for layer associated with cylinder surface coordinates
$\overline{G}_{xy}$	effective shear modulus of cylinder wall
K_{ij}	stiffness of cylinder wall associated with bending-extension coupling
l	length of cylinder
M_x	bending-moment resultant
m_1,m_2	auxiliary constants associated with shear stress in a generally orthotropic layer (see eq. (B1))
N_x,N_y	axial and circumferential load resultants
N_{xy}	shear stress resultant
$\overline{N}_{xy}$	applied shear stress resultant at boundary of shell
p	internal pressure
R	radius of cylinder
S	allowable yield strength in shear for unidirectional layer
$\overline{T}$	applied torque
t	thickness of tube wall
u,v,w	displacements of cylinder wall associated with x, y, and z coordinates, respectively
v	volume fraction (always subscripted), ratio of constituent volume to total volume

X,Y	allowable yield strengths in layer parallel and transverse to fibers, respectively
x,y,z	surface coordinates, measured parallel to cylinder axis, perpendicular to cylinder axis and normal to cylinder surface, respectively (see fig. 1)
Z	orthotropic curvature parameter
α	helical winding angle measured from axis of cylinder (see fig. 1)
γ	shearing strain
ϵ	normal strain
ζ_s,ζ_t	correlation factors associated with shear and extension, respectively (see eqs. (1))
κ	change in curvature
μ	Poisson's ratio
μ_L,μ_T	Poisson's ratios of a layer associated with extension induced by inplane loading parallel and perpendicular to fiber direction, respectively
μ_x,μ_y	Poisson's ratios of a layer associated with extension induced by loading parallel and perpendicular to axis of cylinder, respectively
$\overline{\mu}_x$	effective Poisson's ratio of cylinder wall associated with axial loading
ρ	density of material
σ	normal stress
τ	shear stress
$\overline{\tau}_{xy}$	applied average shear stress

Subscripts:

B	quantities associated with buckling
f	fiber property
i	ith layer
m	matrix property
L	fiber direction
T	direction transverse to fiber
v	void
max	maximum
x	x-direction
y	y-direction, yield

Superscript:

T	total

A subscript preceded by a comma denotes differentiation with respect to the subscript. Bars over symbols denote applied loads at the boundary.

EXPERIMENTAL INVESTIGATION

Test Specimens

The winding geometry of the test specimens of the present investigation is indicated in figures 1 and 2. Figure 1 shows the convention used in describing the winding angles ($\pm\alpha$) as well as the basic coordinate system (x and y) and the sign convention for a positive torque $\overline{T}$. The two types of winding configurations investigated are shown in the photomicrographs presented in figure 2. The line of sight for the figure was the y-axis so that cross sections of circumferentially wound filaments project as circles. The configuration with all helical wraps (fig. 2(a)) is composed of 10 layers wrapped in the

sequence $+\alpha, -\alpha, +\alpha, -\alpha, +\alpha, -\alpha, +\alpha, -\alpha, +\alpha, -\alpha$. The configuration with alternating helical and circumferential wraps (fig. 2(b)) is composed of 12 layers wound in the sequence $+\alpha, -\alpha, 90, +\alpha, -\alpha, 90, +\alpha, -\alpha, 90, +\alpha, -\alpha, 90$. In both configurations, all layers were approximately equal in thickness. An unusual feature of the test specimens was that they did not contain filament crossovers or weaving which customarily occur in the filament winding of cylinders (see, for example, ref. 10, p. 50); thus, each layer had only unidirectional filaments. The two photomicrographs shown in figure 2 also show the irregular fiber spacing and the white, resin-rich areas which are typical of glass filament-wound structures. The dark areas in the figure are believed to have resulted from nonuniform polishing of the specimen and may be an indication of void content.

The test specimens were wet wound from E glass and ERL 2256 epoxy as long tubes which were cured at elevated temperature. The properties of the constituent materials and the cure cycle are given in table I. The tabulated values of matrix modulus and matrix density were obtained from 7.6-cm (3-inch) diameter by 15.2-cm (6-inch) long blocks of resin which were tested in compression. The density and modulus of glass and Poisson's ratios shown are representative values for these materials. Four test specimens were cut from each long tube. Two of the specimens were employed in the investigation described herein. The other two specimens were used in a compressive strength investigation. Each test specimen had the following nominal dimensions: 7.6-cm (3-inch) inside diameter, 18-cm (7-inch) total length, and a total wall thickness of 0.152 cm (0.06 inch). There were 24 helically wrapped specimens with wrap angles varying from 15° to 90° in 15° increments and 12 specimens with alternating helical and circumferential wraps with wrap angles of 15°, 30°, and 45°.

Measured geometry and constituent volume fractions for each test specimen are presented in tables II and III. The two torsion specimens cut from each long tube are numbered successively as 1 and 2, 3 and 4, and so forth in the tables. The helical angles $\pm\alpha$ and the circumferential angles on each specimen were measured from photographs obtained by wrapping photographic film around the circumference of the long tube and illuminating the inside of the tube. The values of wall thickness t shown are the average of several random measurements on each specimen. Scatter in thickness measurements was generally about ±5 percent of values listed in tables II or III although, in a few specimens, deviation of ±6 to ±12 percent existed. (See values of t marked with an asterisk in tables.)

The tabulated values of fiber volume fraction v_f and matrix volume fraction v_m are averages obtained for four coupons cut from the walls of each test specimen. In order to determine v_f and v_m in a manner such that void volume fraction could be estimated, the total volume of each coupon was obtained by comparing the weight of the coupon in air with the weight of the coupon submerged in water. Then burnout tests of 3-hour duration

at 866 K (1100° F) were conducted on each coupon to obtain its glass and matrix material content. The difference between unity and the sum of average glass and average matrix volume fractions was used as an estimate of void content. Scatter in v_f and v_m between coupons of the same specimen was about ±3 percent of the values in tables II and III. Since the void content v_v was obtained as the difference of two large numbers, the tabulated values are probably accurate only to the nearest hundredth.

Test Procedures

To prepare the specimens for torsion testing, the ends of each specimen were reinforced with a 0.17- by 5-cm (1/16- by 2-inch) aluminum-alloy split ring bonded to the external surface of the tube with a room-temperature curing epoxy. The addition of end reinforcement resulted in a test-section length of about 7.6 cm (3 inches). The specimens were tested in a torsion testing machine of 6.8 kN-m (60 000 in-lb) capacity at the Langley Research Center. One end of each specimen was mounted to the stationary head of the machine. The other end was attached to the rotating head which induced a torque determined by a sensitive weighing system. Before each test, the gripping chucks of the torsion machine were carefully alined to ensure that the loading transferred to the test specimen would be pure torsion. The specimen was adapted to the chucks by inserting an accurately machined plug in each end to a depth of about 4.8 cm $\left(1\frac{7}{8} \text{ inches}\right)$. The plugs were carefully shimmed for axial alinement and were attached to the specimen by screws. The aluminum inserts and split rings can be seen in the test setup shown in figure 3.

To measure shearing strains, four wire-resistance-type strain rosettes were bonded to the external surface of the tube. Three-gage 45° rosettes were employed and the central gage was alined parallel to the axis of the tube. (See fig. 3(b).) The two orthogonal gages were used to measure the principal normal strains whereas the central gage was used to detect any axial strains. In order to determine the relative angle of twist of two sections normal to the tube axis, most of the specimens were equipped with two parallel steel rods. Each rod (0.48-cm (3/16-inch) diameter) was mounted in two tightly fitting holes drilled through the walls of the specimen in such a manner that the mounted rods passed diametrically through the specimen. The two rods were spaced about 6.4 cm $\left(2\frac{1}{2} \text{ inches}\right)$ apart. The relative angle of twist of one rod with respect to the other was determined by measuring deflections of the ends of the rods with four deflection transducers (linear variable differential transformers). In figure 3(a) the two transducers on the near side of the specimen are shown.

After completion of tests of the 45° tubes with circumferential wraps, a review of the data suggested that some of the specimens might be developing buckles before failure. Therefore, eight of the tubes (one from each of the remaining configurations) were instrumented with 20 additional single-element strain gages. These gages were located in

back-to-back pairs on the inner and outer surfaces of the tube and were alined with the direction of principal compressive stress so that they would act as buckle detectors. In order to obtain strengths of the tubes in the absence of stress concentration effects, these eight tubes were not drilled to accommodate the rods for measurements of the relative angle of twist.

Two types of loading tests were conducted. Because some nonlinearity in shear stress-strain behavior was anticipated, a preliminary test up to a maximum torque of 68 N-m (600 in-lb) was conducted on each specimen to determine the initial shearing modulus. Then, a test to failure was conducted with a single cycle of load. The loading rate for each test was essentially constant except at the onset of initial loading and during failure. These rates were approximately 0.11 N-m/s (60 in-lb/min) for the preliminary test and 1.1 N-m/s (600 in-lb/min) for the test to failure. During the tests, data were recorded at a virtually continuous rate on the Langley central digital data recording system.

Test Results

Stress-strain behavior.- The data obtained during the tests were reduced and plotted by computer as shear stress-strain curves for each specimen. A sample plot of strain data taken from the orthogonal gages of the rosettes during the failure tests of specimen number 2 is presented in figure 4. The magnitude of the applied shear stress $\bar{\tau}_{xy}$ is plotted against the shear strain γ_{xy}. The applied shear stress $\bar{\tau}_{xy}$ was obtained from the applied torque $\bar{\tau}$, by using Bredt's formula with the tube mean radius, and the shear strain γ_{xy} was obtained by doubling the magnitude of the orthogonal strain-gage reading. Data from the central axial gage of the rosettes indicated that for all practical purposes, a state of pure shear was induced in the test section of each specimen. In figure 4, the curves depict data from the orthogonal gages plotted so that tensile strain gages alternate with the compression gages; each pair of gages is from the same rosette. Note that the gages have a nonlinear response which suggests that some yielding (or degradation of the composite material) has taken place. Various degrees of nonlinearity in such stress-strain curves were observed, depending on the helical wrap angle of the specimen.

A further illustration of the relative nonlinear behavior of the test specimens is given by the shear stress-strain curves presented in figure 5. Those curves are plots showing shear strain obtained from the data of a typical single orthogonal gage of a rosette for one specimen in each α-group. For the helically wound specimens, considerable nonlinearity occurred in the 15°, 75°, and 90° test specimens as illustrated in figure 5(a). For the helically and circumferentially wound specimens, the 15° tubes showed most of the nonlinearity. (See fig. 5(b).) The major difference between the two winding configurations, however, is the maximum shearing strain measured in configurations with the same helical winding angle. Note from figures 5(a) and 5(b) that for specimens with 15° and 30°

helical windings, those with circumferential windings were able to sustain about twice the maximum shearing strain experienced by the all helically wound specimens. Thus, the ability of helically wrapped tubes to withstand large nonlinear strains under torsional loading appears to be considerably enhanced by the addition of interspersed circumferential wraps.

Similar trends in stress-strain behavior were observed by studying the relative angle of twist as determined from the deflection transducer data. The correlation of strain-gage data with reduced deflection transducer data indicated that the strain-gage data were a good overall measure of specimen behavior. Because of rigid-body translations and rotations resulting from apparent slippage and testing machine motor vibrations, the response of individual deflection transducers was not well behaved. The rigid-body deflections of the steel rods were on the order of 4 to 5 times the relative deflection and thus the relative rotation measurements represent small differences of large numbers. It is felt therefore that the relative rotation data are less accurate than the strain-gage data, and hence are not presented.

The average initial slope of stress-strain curves of the type shown in figure 4 for failure tests were compared with similar plots from the preliminary tests at low loadings. The preliminary test data were linear and the stress-strain curve slopes were in good agreement with the failure test data as well as with the relative rotation data. Average values of the initial slope of shear modulus $\overline{G}_{xy}$ are given in tables IV and V for the two winding configurations. Strain values employed in computing modulus were corrected for the transverse gage sensitivity of the rosette by using recommended factors supplied with the gages. Scatter in modulus indicated by individual gages was about ±8 percent of the values shown in the tables. Also shown in tables IV and V are the average applied shear stress $\overline{\tau}_y$ corresponding to yielding as conventionally defined in uniaxial tension tests of metals. The values were obtained by constructing the linear stress-strain curve offset at 0.2-percent shear strain on each of the stress-strain curves (see fig. 4) and averaging the values of stress at the intersections with the strain-gage data curves. The absence of values for $\overline{\tau}_y$ in tables IV and V indicates that strain values for the specimen at failure were not large enough to define the offset yield.

Failure.- The test specimens failed catastrophically at the maximum torques $\overline{T}_{max}$ and shear stresses $\overline{\tau}_{max}$ presented in tables IV and V. Two types of fracture patterns were observed on the test specimens as shown in figure 6. In the helically wound specimens, a line of separation occurred that ran parallel to the filaments loaded in tension (the $+\alpha$ line of fig. 1). The fracture line can be seen on the tubes with 60° and 75° windings shown in figure 6. For the tubes with circumferential windings, the fracture pattern was a band rather than a line and complete separation was not evident. The direction of the band was only approximately parallel to the helical filaments stressed in

tension. The fracture band can be seen in the tubes with 15° windings shown in figure 6 by observing the disrupted lines of reflected light and the areas of lighter color. The lighter color gives evidence of delamination occurring under the external surface of the tube. A close-up view of the appearance of the failure band under loading is given in figure 3(b). The band appears as a ripple line so that filaments with negative winding angles ($-\alpha$ in fig. 1) are wrinkled. In figure 3(b) failure appears to emanate from one of the holes accommodating a steel rod. However, in many other instances, the failure line or band did not include the rod holes. Furthermore, the specimen without holes in the same α-group had a shear strength similar to specimens with holes. Thus, there appears to be no experimental evidence that stress concentration effects introduced by the rod holes had any deleterious effect on the torsional strength of the tubes.

In some of the specimens, a buckle pattern was observed before the final fracture pattern developed. Additional evidence of buckling was obtained by observing strain reversal in the strain gage data from the specimens which were instrumented to detect buckling deformations. An example of stress-strain data with strain-reversal trends is presented in figure 7. The data shown are for specimen number 10 ($\alpha = 45°$) and are taken from strain rosettes plotted in the same manner as in figure 4. From a comparison of the data of figures 4 and 7, it appears that buckling occurred in specimen 10 whereas specimen 2 experienced a material failure. On the basis of studies of stress-strain behavior near failure, specimens in which significant strain-reversal behavior occurred are identified in tables IV and V.

An additional observation during the loading history of the test specimens should be noted. Each specimen emitted several cracking sounds during the strength test. In some cases these noises were accompanied by a drop in applied load which upon further twisting was followed by total recovery of load along the same stress-strain curve. For a few tests the noise level and specimen acceleration were recorded; however, there was no correlation between these measurements and the stress-strain characteristics already discussed. Other investigators have reported similar unsuccessful correlation attempts. It seems that, at present, there is no satisfactory method of assessing the significance of this localized cracking on the structural integrity of composite materials.

COMPARISON OF TEST DATA WITH ANALYSIS

Structural Stiffness

The structural stiffnesses of the tubes were obtained analytically from an analysis of the stresses and deformations in a finite-length generally orthotropic cylindrical shell loaded in torsion. The term "generally orthotropic" is used to describe the character of the helical layers at $+\alpha$ and $-\alpha$ which are such that their principal axes of orthotropy

(the directions parallel and transverse to the fibers) are not parallel or perpendicular to the cylinder axis. (See, for example, ref. 1.) The analysis revealed that the effects of restraints at the boundary of the shell should be very localized; therefore, a membrane state of stress should yield accurate stresses and deformations over most of the shell. The details of the analysis are outlined in appendix B.

In order to estimate the structural stiffnesses of the tubes from the properties of the glass and epoxy constituents (see table I), the elastic constants along coordinates associated with the filaments were computed from the Halpin-Tsai equations discussed in reference 8. These equations are relatively simple to employ and have been empirically correlated with trends from elasticity solutions treating idealized arrays of inclusions in a matrix (for example, ref. 1). If the subscript L denotes a direction parallel to the fiber axes and the subscript T, a direction perpendicular to the fibers, the equations employed for elastic constants for a unidirectional layer can be written as

$$\left.\begin{aligned} E_L &= v_f E_f + v_m E_m \\ \mu_L &= v_f \mu_f + v_m \mu_m \\ E_T &= E_m \frac{1 + \zeta_t \eta_t v_f}{1 - \eta_t v_f} \\ \mu_T &= E_T \frac{\mu_L}{E_L} \\ G_{LT} &= G_m \frac{1 + \zeta_s \eta_s v_f}{1 - \eta_s v_f} \end{aligned}\right\} \qquad (1)$$

with

$$\eta_t = \frac{\frac{E_f}{E_m} - 1}{\frac{E_f}{E_m} + \zeta_s}$$

$$\eta_s = \frac{\frac{G_f}{G_m} - 1}{\frac{G_f}{G_m} + \zeta_s}$$

where

$$\zeta_s = 3.5$$

$$\zeta_t = 3.0$$

In equations (1), ζ_t and ζ_s are empirical correlation factors associated with transverse normal load and shear load respectively; the values assigned to these parameters were selected to agree with experimental results of the present investigation.

As outlined in appendix B, the elastic constants for the unidirectional layer are transformed into elastic constants associated with the x,y coordinates. (See fig. 1.) The structural stiffnesses of the shell are then obtained by inversion of the strain-stress law and integration over the total tube wall thickness. The effective shear moduli of the wall $\overline{G}_{xy}$ of the tube can be computed from the integrated shear stiffness. (See eq. (B19).) A comparison of the analytically and experimentally determined values of the shear modulus is presented in figure 8. The calculated curves were computed for a nominal glass volume fraction of 0.63 and are compared with data with similar volume fractions. Calculations for specific specimens with actual volume fractions are presented in tables IV and V. Based on the results shown, it can be seen that the computed results are in good agreement with experimental values, the maximum deviation being about 10 percent.

Torsional Buckling

As previously mentioned, certain experimental observations suggested that some of the test specimens may have buckled prior to final fracture. The torsional buckling stress of the test specimens was estimated from an analysis for an orthotropic shell developed by Chao in reference 11. The analysis is similar to the buckling solution presented by Cheng and Ho in reference 12. Minor differences in the two solutions are associated with the use of Timoshenko's shell theory by Chao and Flügge's shell theory by Cheng and Ho. The theory rigorously accounts for the generally orthotropic character of the tube helical-layer configurations. Structural stiffnesses employed in the determination of the buckling strength were derived from the Halpin-Tsai equations and the procedures described in appendix B. The buckling computations were performed with a computer program based on reference 11.

The significance of boundary conditions on the predicted torsional buckling stress of the test specimens was investigated by making buckling calculations for both clamped and simply supported cylinders. The boundary conditions prescribed during buckling were those usually employed in classical theory (for example, ref. 13) and can be written as follows:

For simply supported cylinders,

$$N_{x,B} + \overline{N}_{xy} \frac{\partial u_B}{\partial y} = v_B = w_B = M_{x,B} = 0 \qquad (2)$$

For clamped cylinders,

$$\mu_B = N_{xy,B} + \frac{M_{xy,B}}{R} = w_B = \frac{\partial w_B}{\partial x} = 0 \tag{3}$$

The results of the computations are presented in figure 9 where the predicted values of shear stress corresponding to elastic torsional instability are compared with the experimental torsional strength of the tube. The torsional strength was defined as either the 0.2-percent offset yield stress $\bar{\tau}_y$ or the maximum shear stress $\bar{\tau}_{max}$ of specimens for which the 0.2-percent offset yield was not defined. The buckling computations are based on a nominal volume fraction and are for a shell with a length corresponding to the unsupported test-section length of 7.6 cm (3 inches). The buckling results presented correspond to 0.67 times the theoretical value obtained from Chao's work. This reduction in theoretical results has been suggested for moderately long cylinders in reference 14, and it is believed to be appropriate for the test specimens. Although the specimens are relatively thick walled shells (R/t = 30), they appear to behave as moderately long orthotropic shells, if the curvature parameter Z is used as a length measure. For orthotropic shells, the parameter is a function of structural stiffness as well as of geometry (ref. 15) and can be written as

$$Z = \sqrt{\frac{C_{11}\ell^4}{12D_{22}R^2}} \tag{4}$$

where C_{11} is the axial extensional stiffness and D_{22} is the circumferential bending stiffness. For the test specimens, Z ranges from 70 to 180, which is in the moderate-length range. Studies of isotropic cylindrical shells of similar Z (see refs. 16 and 17) have suggested that theoretical torsion buckling loads should be reduced to account for imperfection sensitivity.

The results shown in figure 9 indicate that strengths for tubes with only 30° windings and those with only 45° windings correlate with the buckling predictions. The observed strengths for other helical winding angles and for the tubes with both helical and circumferential windings are significantly lower than the buckling predictions. On the basis of these trends, it appears that most of the specimens were not subject to elastic instability. The strain-reversal trends as indicated in table IV substantiate the buckling behavior of all the tubes with only 45° windings and for one of the tubes with only 30° windings. Hence, it is believed that tubes with only 45° windings failed by elastic instability. It is not obvious whether the tubes with only 30° windings buckled elastically. The strain-reversal trends noted for other tubes in tables IV and V occurred at strains well beyond

those corresponding to 0.2-percent offset yield stresses and are believed to be the consequences of stiffness degradation and inelastic buckling at loads corresponding to large nonlinear strains.

Yielding of Layers

Stress analysis.- The elastic stresses necessary to cause yielding in the layers of the test specimens were investigated. By using equations (1) and the orthotropic shell analysis described in appendix B, stresses in each layer were determined in the cylindrical surface coordinates (x,y in fig. 1). The stresses were then resolved into components along axes parallel and transverse to the fibers (L,T) by employing the usual stress transformation equations.

Results for the average stresses σ_L, σ_T and τ_{LT} in each layer are presented in figures 10 and 11. The curves shown indicate the changes in these stresses with helical winding angle. Because the membrane stresses in each layer are linear with respect to applied stress (see appendix B), the stresses shown have been normalized with respect to the applied shear stress $\bar{\tau}_{xy}$. In general, for the torque shown in figure 1 (that is, $+\bar{T}$ and $+\tau_{xy}$), the relative state of stress in the helically wound layers at $+\alpha$ and $-\alpha$ can be distinguished in sketch (a):

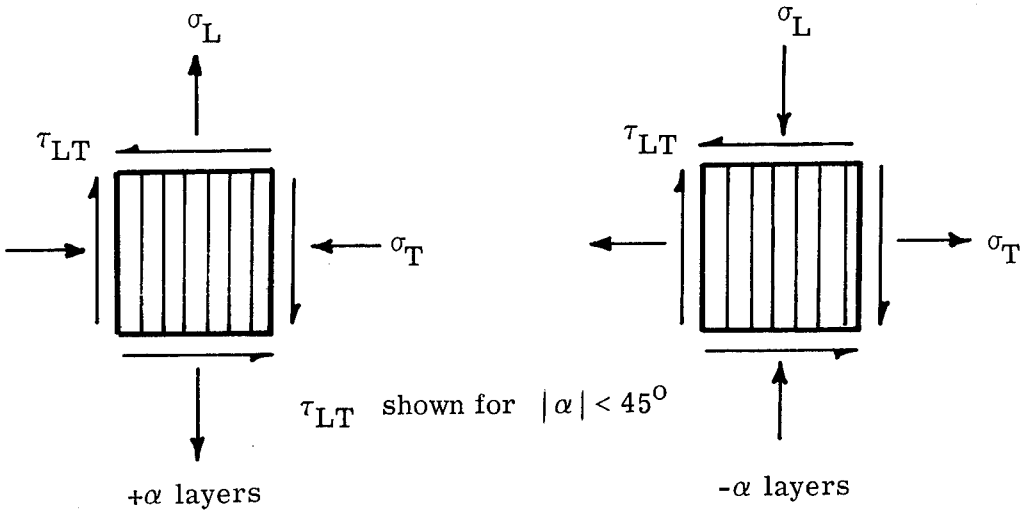

Sketch (a)

The circumferential layers, of course, are always in a state of pure shear.

Two conclusions can be drawn from the results presented in figures 10 and 11. The first is that the presence of transverse tensile stress in the $-\alpha$ layers is likely to cause yielding in the matrix in these layers before yielding of the $+\alpha$ layers. The conclusion is based on the observation that tests of circumferentially wound tubes in tension and

compression have indicated that yielding occurs in tensilely stressed tubes at significantly lower stresses. If yielding does occur in the $-\alpha$ layer, the presence of compressive stresses in the filament direction would be expected to cause microbuckling or wrinkling of the filaments since the yielded matrix presumably would have diminished capability to support the filaments. On the other hand, the $+\alpha$ layer is inherently more stable because the filaments in this layer are loaded in tension. Thus, yielding of the matrix because of transverse compression stresses is not likely to precipitate filament failure. Hence, it is concluded that the $-\alpha$ layers are the weakest elements in the composite structure.

The second conclusion is that the critical stress interactions in individual layers are associated with shear stresses and stresses transverse to the filament. From figure 10, it can be seen that the maximum stress in the filament direction σ_L is at most $1\frac{1}{2}$ times the applied shear stress. From table V the maximum applied shear stress was about 200 MN/m^2 (30 ksi). Since tensile or compressive strengths of tubes with axially oriented filaments are roughly six or seven times this value, the influence of the magnitude of stresses in the filament direction should be relatively small.

Orthotropic yield criteria.- With the stresses in each layer of the tube expressed in terms of the stress ratios $\sigma_L/\bar{\tau}_{xy}$, $\sigma_T/\bar{\tau}_{xy}$, and $\tau_{LT}/\bar{\tau}_{xy}$, stresses at yield were determined from various forms of orthotropic yield criteria. The more widely used orthotropic yield criteria proposed in the literature can be written in the general form:

$$\tau_y^2 = \frac{1}{\left(\frac{\sigma_L/\bar{\tau}_{xy}}{X}\right)^2 - a\frac{\left(\sigma_L/\bar{\tau}_{xy}\right)\left(\sigma_T/\bar{\tau}_{xy}\right)}{X^2} - b\frac{\left(\sigma_L/\bar{\tau}_{xy}\right)\left(\sigma_T/\bar{\tau}_{xy}\right)}{|X||Y|} + \left(\frac{\sigma_T/\bar{\tau}_{xy}}{Y}\right)^2 + \left(\frac{\tau_{LT}/\bar{\tau}_{xy}}{S}\right)^2} \qquad (5)$$

where τ_y is the value of the applied shear stress $\bar{\tau}_{xy}$ at yielding of the tube, X and Y are yield strengths of a unidirectional layer in directions parallel and transverse to the filaments, and S is the yield strength in shear associated with the filament coordinates When various values are assigned to the coefficients a and b, equation (5) will reduce to forms proposed in the literature as indicated in the table:

a	b	Source	Reference
0	0	ANC-18	18
1	0	Hill	19
0	1	Norris	20
0	Empirical	Chamis	21

In the analysis, values assigned to the strengths X, Y, and S were as follows:

Strength	Tension		Compression		Shear	
	MN/m^2	ksi	MN/m^2	ksi	MN/m^2	ksi
X	1379	200	1379	200		
Y	41	6	138	20		
S					41	6

The strengths for Y are based on several compression tests and a single tension test on circumferentially wound tubes similar to the test specimens. The strength S is based on the present tests of tubes with only 90° windings whereas X is a conservative nominal value.

Calculations for yield strengths indicated that terms involving X in the yield criterion are negligible except for helical wrap angles near 45°. This trend is a consequence of the stress distributions previously discussed. Because of this effect, a simplified form of the yield criterion

$$\tau_y^2 = \frac{1}{\left(\frac{\sigma_T/\bar{\tau}_{xy}}{Y}\right)^2 + \left(\frac{\tau_{LT}/\bar{\tau}_{xy}}{S}\right)^2} \tag{6}$$

appeared to be appropriate for the present study.

A comparison of the experimental torsional strengths corresponding to the 0.2-percent offset yield stress (or maximum stress when the 0.2-percent offset yield could not be defined (tables IV and V)) and analytical yield stress predictions for a nominal volume fraction of 0.63 is given in figure 12. Data for 45° helically wrapped tubes have been omitted since buckling calculations and experimental observations suggest that these specimens failed by buckling. The solid curves shown correspond to the simplified yield criterion (eq. (6)) for the $+\alpha$, $-\alpha$, and 90° layers of the cylinders. The dashed curves correspond to the more complex criterion (eq. (5)) as proposed by Norris (a = 0, b = 1) and have been included to illustrate the significance of the X-terms in the yield criteria. The curves shown verify that yielding should occur in the $-\alpha$ layer before it occurs in the $+\alpha$ layer because of the weakness of the $-\alpha$ layer in transverse tension. Substantial differences exist between yielding predictions in the $+\alpha$ layers and the $-\alpha$ and 90° layers. The experimental data would be expected to lie between the yield predictions for $+\alpha$ and other layers, since local yielding in one layer is likely to shift load to other layers and cause a reduction in the yielding strength of the multilayered tube.

The data shown in figure 12, however, appear to correlate with the $+\alpha$ curves. This unexpected result can only be explained by postulating that yielding in the $-\alpha$ layer is a relatively mild phenomenon. As discussed previously, the compressive stresses in the $-\alpha$ layer are likely to cause microbuckling or wrinkling of the filaments. Except for the surface layer, the $-\alpha$ layers are sandwiched between two stable layers in which at least one layer (the $+\alpha$ layer) has filaments stretched in tension. Presumably, this condition permits the multilayer composite to carry substantially larger loads after initial local yielding. The large nonlinear strains observed in the helically and circumferentially wound specimens also demonstrate that unusual behavior can occur in complex multilayered configurations. In the present calculations, if yielding in the $-\alpha$ layers and 90° layers of the tubes is ignored, the present data could be correlated reasonably well with orthotropic yield criteria. Alternatively, the data could also be correlated with analysis if larger values of the transverse tensile yield stress Y and the shear stress S were employed in the analysis so that yielding in the helical ($+\alpha$ and $-\alpha$) and circumferential layers was coincident. The higher values, however, are believed to be unrealistic and are not advisable for design. Thus, as applied herein, the orthotropic yield criteria appear to give unduly conservative predictions of the behavior of the test specimens.

The conservativeness of similar applications of orthotropic yield criteria has also been noted in correlating compression data (ref. 22) for glass-epoxy tubes. The present study and referenced studies raise serious questions as to the engineering applicability of the orthotropic yield criteria based on elastic stress analysis to estimate compressive and shear strengths of multilayered composites. It appears that a more intimate knowledge of the postyielding behavior of composite structures is required before reasonable estimates of maximum strengths can be made. Some recent studies (refs. 23 and 24) have suggested that orthotropic yield criteria can be applied to study progressive layer failures. Most of the successes with postyielding analyses, however, have been obtained with layers loaded in tension; thus, applications to shear and compressive loadings deserve further study.

CONCLUDING REMARKS

The results of torsion tests to failure conducted on 36 multilayered filament-wound tubes have been reported. Shear stress-strain data obtained during the tests indicated various degrees of nonlinearity (yielding) depending on the helical orientation of filaments in the tubes. Shear moduli based on the initial slope of the stress-strain curves were in good agreement with analytical predictions from a semiempirical theory employing constituent material properties. Fracture of helically wound tubes appeared to be accompanied by separation lines parallel to filaments stressed in tension. Fracture patterns in tubes with interspersed helically and circumferentially wound layers appeared to be a band (rather than a separation line) in which delamination was evident. Specimens with

interspersed circumferential windings exhibited the capability of carrying much larger postyielding strains than comparable specimens with only helical windings. Specimens with only 45° windings exhibited strain reversal near failure and are believed to have buckled. The maximum strength of these tubes were in agreement with torsional buckling predictions based on orthotropic theory when theoretical values were reduced to account for imperfection sensitivity. Shear stress data at yield (as defined by 0.2-percent offset strain) or maximum load were compared with yield strengths obtained from orthotropic yield criteria and elastic stress analysis. Computed results indicate that the yield criteria do not adequately explain the behavior of helical layers in the test specimens which are loaded in tension transverse to the filaments. Data could be correlated only when yielding of certain layers was ignored or when unrealistically large values of transverse tensile and shear strengths were employed in the strength analysis.

Langley Research Center,
National Aeronautics and Space Administration,
Hampton, Va., May 26, 1971.

APPENDIX A

CONVERSION OF U.S. CUSTOMARY UNITS TO SI UNITS

The International System of Units (SI) was adopted by the Eleventh General Conference on Weights and Measures in 1960. (See ref. 9). Conversion factors for the units used herein are given in the following table:

Physical quantity	U.S. Customary Unit	Conversion factor (*)	SI Unit
Length	in.	0.0254	meters (m)
Temperature	(^{o}F + 460)	5/9	kelvin (K)
Force	lbf	4.448	newtons (N)
Density	lbm/ft^3	16.02	kilograms per cubic meter (kg/m^3)
Stress, pressure . . .	$psi = lbf/in^2$	6895	newtons per square meter (N/m^2)
Torque	in-lbf	0.1130	newton-meters (N-m)

*Multiply value given in U.S. Customary Unit by conversion factor to obtain equivalent value in SI Unit.

Prefixes to indicate multiple of units are as follows:

Prefix	Multiple
kilo (k)	10^3
mega (M)	10^6
giga (G)	10^9
centi (c)	10^{-2}
micro (μ)	10^{-6}

APPENDIX B

STRESS DISTRIBUTION IN A GENERALLY ORTHOTROPIC CYLINDRICAL SHELL

Stress distributions in the test specimens were investigated by developing a solution for axisymmetric deformation in a multilayered, orthotropic, cylindrical shell loaded in torsion and axial compression. The orthotropicity in the cylinder layers was such that neither of the principal axes of each layer was assumed to be alined with the cylinder axis. The details of the general solution are rather lengthy and are not presented herein. A general conclusion of the investigation was that a state of membrane stress is developed under torsional and compressive loadings over a large area of the tubes and that effects of restraint at the boundaries of the shell are very localized. The results presented herein are intended to document those equations pertinent to analytical estimates of the composite wall stiffnesses of the tube and the stress distribution in each of the layers of the tube.

In the analysis, the elastic constants for each of the layers of the tube were taken to be generally orthotropic so that Hooke's law for the ith layer can be written as

$$\begin{bmatrix} \epsilon_x{}^T \\ \epsilon_y{}^T \\ \gamma_{xy}{}^T \end{bmatrix}_i = \begin{bmatrix} \frac{1}{E_x} & -\frac{\mu_y}{E_y} & -m_1 \\ -\frac{\mu_x}{E_x} & \frac{1}{E_y} & -m_2 \\ -m_1 & -m_2 & \frac{1}{G_{xy}} \end{bmatrix}_i \begin{bmatrix} \sigma_x \\ \sigma_y \\ \tau_{xy} \end{bmatrix}_i \tag{B1}$$

where the superscript T denotes the total strain in the layer (bending + extension). The elastic constants in the x,y coordinate system (fig. 1) are related to properties perpendicular and parallel to the fiber direction by the following transformation equations (ref. 25)

$$\left.\begin{aligned}
\frac{1}{E_x} &= \frac{\cos^4\alpha}{E_L} + \left(\frac{1}{G_{LT}} - \frac{2\mu_L}{E_L}\right)\sin^2\alpha\cos^2\alpha + \frac{\sin^4\alpha}{E_T} \\
\frac{1}{E_y} &= \frac{\sin^4\alpha}{E_L} + \left(\frac{1}{G_{LT}} - \frac{2\mu_L}{E_L}\right)\sin^2\alpha\cos^2\alpha + \frac{\cos^4\alpha}{E_T} \\
\frac{1}{G_{xy}} &= \frac{1}{G_{LT}} + \left(\frac{1+\mu_L}{E_L} + \frac{1+\mu_T}{E_T} - \frac{1}{G_{LT}}\right)\sin^2 2\alpha \\
\frac{\mu_x}{E_x} &= \frac{\mu_y}{E_y} = \frac{\mu_L}{E_L} - \frac{1}{4}\left(\frac{1+\mu_L}{E_L} + \frac{1+\mu_T}{E_T} - \frac{1}{G_{LT}}\right)\sin^2 2\alpha \\
m_1 &= \left[\frac{\sin^2\alpha}{E_T} - \frac{\cos^2\alpha}{E_L} + \frac{1}{2}\left(\frac{1}{G_{LT}} - \frac{2\mu_L}{E_L}\right)\cos 2\alpha\right]\sin 2\alpha \\
m_2 &= \left[\frac{\cos^2\alpha}{E_T} - \frac{\sin^2\alpha}{E_L} - \frac{1}{2}\left(\frac{1}{G_{LT}} - \frac{2\mu_L}{E_L}\right)\cos 2\alpha\right]\sin 2\alpha
\end{aligned}\right\} \tag{B2}$$

As discussed in the text, the elastic constants associated with the unidirectional layer (L and T coordinates) were estimated from the Halpin-Tsai equations. The stresses in the ith layer of the shell can be found from the inverse of equation (B1) as

$$\begin{bmatrix} \sigma_x \\ \sigma_y \\ \tau_{xy} \end{bmatrix}_i = \begin{bmatrix} B_{11} & B_{12} & B_{16} \\ B_{12} & B_{22} & B_{26} \\ B_{16} & B_{26} & B_{66} \end{bmatrix}_i \begin{bmatrix} \epsilon_x{}^T \\ \epsilon_y{}^T \\ \gamma_{xy}{}^T \end{bmatrix}_i \tag{B3}$$

The shell was considered to experience only axisymmetric deformation. By using the Donnell-von Karman assumptions, the strains appearing in equations (B3) can be written in terms of the tangential and normal displacements u, v, and w as

$$\left.\begin{aligned} \epsilon_x{}^T &= \epsilon_x + z\kappa_x = u_{,x} + \frac{1}{2} w_{,x}{}^2 - z w_{,xx} \\ \epsilon_y{}^T &= \epsilon_y = \frac{w}{R} \\ \gamma_{xy}{}^T &= \gamma_{xy} = v_{,x} \end{aligned}\right\} \tag{B4}$$

To employ shell theory, it is convenient to integrate equations (B3) across the shell wall and introduce the following stress resultants:

$$\begin{bmatrix} N_x \\ N_y \\ N_{xy} \\ M_x \end{bmatrix} = \begin{bmatrix} C_{11} & C_{12} & C_{16} & K_{11} \\ C_{12} & C_{22} & C_{26} & K_{12} \\ C_{16} & C_{26} & C_{66} & K_{16} \\ K_{11} & K_{12} & K_{16} & D_{11} \end{bmatrix} \begin{bmatrix} \epsilon_x \\ \epsilon_y \\ \gamma_{xy} \\ \kappa_x \end{bmatrix} \tag{B5}$$

where C_{jk}, D_{jk}, and K_{jk}, the structural stiffnesses, associated with extension, bending, and bending-extension coupling, respectively, are defined by

$$\left(C_{jk}, K_{jk}, D_{jk}\right) = \int_{\text{wall}} \left(B_{jk}\right)_i \left(1, z, z^2\right) dz \tag{B6}$$

By use of the Donnell theory, the equilibrium equations for the shell can be written as

$$N_{x,x} = 0 \tag{B7}$$

$$N_{xy,x} = 0 \tag{B8}$$

$$-M_{x,xx} + \frac{N_y}{R} - N_x w_{,xx} = p \tag{B9}$$

where p denotes internal pressure. The general case in which an axial compressive load $\bar{N}_x$ and shear load $\bar{N}_{xy}$ are applied at the boundaries was investigated. For this case equations (B7) and (B8) can be integrated so that

$$N_x = -\bar{N}_x \tag{B10}$$

$$N_{xy} = \bar{N}_{xy} \tag{B11}$$

Equation (B10) together with the first row of matrix equation (B5) imply that

$$\epsilon_x = \frac{K_{11}}{C_{11}} w_{,xx} - \frac{C_{12}}{C_{11}} \frac{w}{R} - \frac{C_{16}}{C_{11}} v_{,x} - \frac{\bar{N}_x}{C_{11}} \tag{B12}$$

If equations (B11) and (B9) are expressed in terms of displacement, and equation (B12) is used to eliminate ϵ_x, the following coupled equations in v and w result:

$$A_1 v_{,x} + A_2 w_{,xx} + A_3 w = P_1 \tag{B13}$$

$$A_2 v_{,xxx} + A_3 v_{,x} + A_4 w_{,xxxx} + A_5 w_{,xx} + A_6 w = P_2 \tag{B14}$$

with

$$A_1 = C_{66} - \frac{C_{16}^2}{C_{11}}$$

$$A_2 = \frac{C_{16} K_{11}}{C_{11}} - K_{16}$$

$$A_3 = \frac{1}{R}\left(C_{26} - \frac{C_{12} C_{16}}{C_{11}}\right)$$

$$A_4 = D_{11} - \frac{K_{11}^2}{C_{11}}$$

$$A_5 = \frac{2}{R}\left(\frac{K_{11} C_{12}}{C_{11}} - K_{12}\right) + \bar{N}_x$$

$$A_6 = \frac{1}{R^2}\left(C_{22} - \frac{C_{12}^2}{C_{11}}\right)$$

$$P_1 = \bar{N}_{xy} + \bar{N}_x \frac{C_{16}}{C_{11}}$$

$$P_2 = \frac{\bar{N}_x C_{12}}{R C_{11}} + p$$

By use of the usual techniques for solving simultaneous ordinary differential equations, a general solution of equations (B13) and (B14) can be found in terms of hyperbolic and trigonometric functions. If the boundary conditions are applied at $x = \pm\frac{l}{2}$ where l is the length of the shell, the nontrivial solution becomes antisymmetric in v and symmetric in w and can be expressed as

$$v = B_1 \sinh \beta x \cos \gamma x + B_2 \cosh \beta x \sin \gamma x + \frac{P_1A_6 - P_2A_3}{A_1A_6 - A_3^2}x \tag{B15}$$

$$w = C_1 \sinh \beta x \sin \gamma x + C_2 \cosh \beta x \cos \gamma x + \frac{P_2A_1 - P_1A_3}{A_1A_6 - A_3^2} \tag{B16}$$

where

$$\beta = \sqrt{\frac{1}{2}\left(\sqrt{\frac{S_3}{S_1}} - \frac{S_2}{2S_1}\right)}$$

$$\gamma = \sqrt{\frac{1}{2}\left(\sqrt{\frac{S_3}{S_1}} + \frac{S_2}{2S_1}\right)}$$

with

$$S_1 = A_1A_4 - A_2^2$$

$$S_2 = A_1A_5 - 2A_2A_3$$

$$S_3 = A_1A_6 - A_3^2$$

Calculations employing the general solutions (eqs. (B15) and (B16)) with clamped or simply supported boundary conditions indicate that in a multilayered tube with alternating layers at $+\alpha$ and $-\alpha$ the boundary conditions are very localized. Hence the membrane displacements contained in the particular solutions of equations (B15) and (B16) should be good approximations with which to determine the state of stress in regions of the shell away from the ends. For the configurations of the present investigation,

$$C_{16} = C_{26} = 0 \tag{B17}$$

Thus for the tube loaded only in torsion, the membrane displacements are

$$\left.\begin{aligned} v &= \frac{\overline{N}_{xy}}{C_{66}}x \\ w &= 0 \end{aligned}\right\} \tag{B18}$$

By using the definition of the stress resultants (B5), the effective shear modulus of the multilayered wall is defined as

$$\overline{G}_{xy} = \frac{\overline{N}_{xy/t}}{\gamma_{xy}} = \frac{C_{66}}{t} \tag{B19}$$

where t is the total thickness of the shell wall. From equations (B18), the stresses in any layer of the cylinder can be computed by employing equations (B3) and (B4).

For configurations similar to those of the present investigation which are loaded only in axial compression, the membrane displacements are

$$\left.\begin{aligned} v &= 0 \\ w &= \frac{C_{12}}{C_{11}} \frac{\overline{N}_x R}{C_{22} - \frac{C_{12}^2}{C_{11}}} \end{aligned}\right\} \tag{B20}$$

The effective axial modulus $\overline{E}_x$ of the multilayered shell is given by

$$\overline{E}_x = -\frac{\overline{N}_{x/t}}{\epsilon_x} = \left(C_{11} - \frac{C_{12}^2}{C_{11}}\right)\left(\frac{1}{t}\right) \tag{B21}$$

The effective Poisson's ratio associated with axial compressive loading can be written as

$$\overline{\mu}_x = -\frac{\epsilon_y}{\epsilon_x} = \frac{C_{12}}{C_{22}} \tag{B22}$$

REFERENCES

1. Tsai, Stephen W.; Adams, Donald F.; and Doner, Douglas R.: Analyses of Composite Structures. NASA CR-620, 1966.

2. Analytical Mechanics Dep., Bendix Corp.: Exploratory Application of Filament Wound Reinforced Plastics for Aircraft Landing Gear. Tech. Rep. AFML-TR-66-309, U.S. Air Force, Dec. 1966. (Available from DDC as AD 806 336.)

3. Grinius, Victor G.: Micromechanics – Failure Mechanism Studies. Proceedings 22nd Annual Technical Conference. SPI Reinforced Plastics Division, Soc. Plastics Industry, Inc., Jan.-Feb. 1967.

4. Holston, A., Jr.; Feldman, A.; and Stang, D. A.: Stability of Filament Wound Cylinders Under Combined Loading. Tech. Rep. AFFDL-TR-67-55, U.S. Air Force, May 1967.

5. Noyes, J. V.; and Jones, B. H.: Crazing and Yielding of Reinforced Composites. AFML-TR-68-51, U.S. Air Force, Mar. 1968. (Available from DDC as AD 839 735.)

6. Bert, Charles W.; Mayberry, Byron L.; and Ray, John D.: Behavior of Fiber-Reinforced Plastic Laminates Under Uniaxial, Biaxial, and Shear Loadings. USAAVLABS Tech. Rep. 68-86, U.S. Army, Jan. 1969. (Available from DDC as AD 684 321.)

7. Puck, A.; and Schneider, W.: On Failure Mechanisms and Failure Criteria of Filament-Wound Glass-Fibre/Resin Composites. Plastics & Polymers, vol. 37, no. 127, Feb. 1969, pp. 33-44.

8. Ashton, J. E.; Halpin, J. C.; and Petit, P. H.: Primer on Composite Materials: Analysis. Technomic Pub. Co., Inc., c.1969.

9. Comm. on Metric Pract.: ASTM Metric Practice Guide. NBS Handbook 102, U.S. Dep. Com., Mar. 10, 1967.

10. Tasi, J.; Feldman, A.; and Stang, D. A.: The Buckling Strength of Filament-Wound Cylinders Under Axial Compression. NASA CR-266, 1965.

11. Chao, Tung-Lai: Minimum Weight Design of Stiffened Fiber Composite Cylinders. AFML-TR-69-251, U.S. Air Force, Sept. 1969.

12. Cheng, S.; and Ho, B. P. C.: Stability of Heterogeneous Aeolotropic Cylindrical Shells Under Combined Loading. AIAA J., vol. 1, no. 4., Apr. 1963, pp. 892-898.

13. Batdorf, S. B.; Stein, Manuel; and Schildcrout, Murry: Critical Stress of Thin-Walled Cylinders in Torsion. NACA TN 1344, 1947.

14. Anon.: Buckling of Thin-Walled Circular Cylinders. NASA SP-8007, 1965. (Revised 1968.)

15. Simitses, George J.: Instability of Orthotropic Cylindrical Shells Under Combined Torsion and Hydrostatic Pressure. AIAA J., vol. 5, no. 8. Aug. 1967, pp. 1463-1469.

16. Budiansky, Bernard: Post-Buckling Behavior of Cylinders in Torsion. Rep. SM-17, Harvard Univ., Aug. 1967. (Available as NASA CR-88232.)

17. Stein, Manuel: Some Recent Advances in the Investigation of Shell Buckling. AIAA J., vol. 6, no. 12, Dec. 1968, pp. 2339-2345.

18. Anon: Design of Wood Aircraft Structures. ANC-18 Bull., Second ed., Munitions Board Aircraft Comm., Dep. Defense, June 1951.

19. Hill, R.: The Mathematical Theory of Plasticity. The Clarendon Press, 1956.

20. Norris, Charles B.: Strength of Orthotropic Materials Subjected to Combined Stresses. Rep. no. 1816, Forest Products Lab., U.S. Dep. Agriculture, July 1950.

21. Chamis, Christos C.: Failure Criteria for Filamentary Composites. NASA TN D-5367, 1969.

22. Card, Michael F.: Experiments To Determine the Strength of Filament-Wound Cylinders Loaded in Axial Compression. NASA TN D-3522, 1966.

23. Noyes, J. V.; and Jones, B. H.: Analytical Design Procedures for the Strength and Elastic Properties of Multilayer Fibrous Composites. AIAA Paper No. 68-336, Apr. 1968.

24. Chiu, Kao Ding: Ultimate Strengths of Laminated Composites. J. Compos. Mater., vol. 3, July 1969, pp. 578-582.

25. Dietz, Albert, G. H., ed.: Engineering Laminates. John Wiley & Sons, Inc., 1949.

TABLE I.- TUBE CONSTITUENT PROPERTIES

(a) International System of Units

Material	E, GN/m^2	μ	ρ, kg/m^3
Type E-HTS 12 and 20 end glass roving	72.40	0.23	2.57
ERL 2256/MPDA epoxy resin Cure: 2 hours at 394 K	4.37	0.40	1.23

(b) U.S. Customary Units

Material	E, ksi	μ	ρ, lbm/cu in.
Type E-HTS 12 and 20 end glass roving	10 500	0.23	0.0930
ERL 2256/MPDA epoxy resin Cure: 2 hours at 250^{o} F	635	0.40	0.0445

TABLE II.- GEOMETRY AND VOLUME FRACTIONS OF HELICALLY WOUND TUBES

[Tube: inside diameter, 7.62 cm (3.00 in.); test section length, 7.62 cm (3.00 in.)]

Specimen	Winding angle, α, deg			t		v_f	v_m	v_v
	Nominal	+	-	cm	in.			
1	15	15	19	0.160	0.0631	0.481	0.495	0.024
2	15	14	18	.160	.0631	.491	.488	.021
3	15	13	17	.151	.0593	.537	.445	.018
4	15	20	17	.148	.0584	.524	.463	.013
5	30	32	30	.144	.0567	.580	.388	.032
6	30	30	31	.144	.0569	.577	.375	.048
7	30	31	32	.168	.0660	.565	.402	.033
8	30	32	30	.168	.0663	.558	.398	.044
9	45	48	46	.136	.0534	.607	.325	.068
10	45	46	48	.131	.0516	.609	.328	.063
11	45	48	45	.130	.0511	.621	.339	.040
12	45	47	50	.136	.0534	.627	.336	.037
13	60	61	62	*.163	*.0641	.651	.278	.071
14	60	61	61	*.157	*.0620	.667	.275	.058
15	60	63	61	.139	.0547	.651	.296	.053
16	60	61	61	.141	.0555	.651	.295	.054
17	75	76	75	*.101	*.0396	.620	.334	.046
18	75	77	77	.102	.0402	.637	.342	.021
19	75	77	77	*.161	*.0633	.585	.367	.048
20	75	76	75	*.164	*.0646	.584	.374	.042
21	90	90		.142	.0559	.633	.324	.043
22	90	89		.143	.0562	.630	.312	.058
23	90	90		*.128	*.0506	.636	.297	.067
24	90	89		*.124	*.0490	.656	.273	.071

*Scatter in t > ±5 percent.

TABLE III.- GEOMETRY AND VOLUME FRACTIONS OF HELICALLY AND CIRCUMFERENTIALLY WOUND TUBES

[Tube: inside diameter, 7.62 cm (3.00 in.); test section length, 7.62 cm (3.00 in.)]

Specimen	Winding angle, α, deg				t		v_f	v_m	v_v
	Nominal	+	-	Circumferential	cm	in.			
25	15, 90	18	16	91	0.157	0.0620	0.604	0.339	0.057
26	15, 90	16	18	90	.157	.0617	.628	.349	.023
27	15, 90	20	18	91	.156	.0614	.603	.360	.037
28	15, 90	20	17	91	.161	.0633	.603	.379	.018
29	30, 90	31	30	91	.149	.0586	.615	.336	.049
30	30, 90	32	31	91	.151	.0594	.616	.345	.039
31	30, 90	31	31	91	*.150	*.0590	.615	.345	.040
32	30, 90	30	33	91	.151	.0594	.604	.345	.051
33	45, 90	48	46	90	.154	.0607	.639	.310	.051
34	45, 90	47	47	89	.155	.0612	.633	.319	.048
35	45, 90	48	46	89	.155	.0611	.661	.324	.015
36	45, 90	46	47	89	.151	.0596	.655	.304	.041

*Scatter in $t > \pm 5$ percent.

TABLE IV.- TEST RESULTS FOR HELICALLY WOUND TUBES

(a) International System of Units

Specimen	Nominal winding angle, α, deg	Shear modulus, $\bar{G}_{xy}$, MN/m^2		Experimental offset yield stress, $\bar{\tau}_y$, MN/m^2	$\bar{T}_{max}$, m-N	$\bar{\tau}_{max}$, MN/m^2
		Experimental	Analytical			
1	15	7300	7564	73.8	1540	101
2	15	7700	7571	71.0	1570	*103
3	15	8100	8067	76.5	1500	105
4	15	8200	8605	78.6	1300	92
5	30	13400	12142		1840	135
6	30	12800	11990		2080	152
7	30	12500	11880		2700	169
8	30	13200	11639		2450	*153
9	45	14400	14059		2230	*174
10	45	15700	14107		2240	*181
11	45	16300	14424		2120	*174
12	45	15400	14500		2170	*170
13	60	14800	13425		1750	113
14	60	15200	13935		1840	123
15	60	14800	13328		1670	128
16	60	14800	13521		1600	121
17	75	10100	9868	70.3	820	88
18	75	9900	9998	65.6	820	87
19	75	9500	8846	66.2	1510	99
20	75	9500	9074	64.8	1530	98
21	90	8100	8757	42.1	620	46
22	90	7900	8688	39.3	560	42
23	90	8800	8826	39.3	470	39
24	90	9300	9301	39.3	540	46

*Significant strain reversal at failure.

TABLE IV.- TEST RESULTS FOR HELICALLY WOUND TUBES – Concluded

(b) U.S. Customary Units

Specimen	Nominal winding angle, α, deg	Shear modulus, $\bar{G}_{xy}$, ksi		Experimental offset yield stress, $\bar{\tau}_y$, ksi	$\bar{T}_{max}$, in.-kips	$\bar{\tau}_{max}$, ksi
		Experimental	Analytical			
1	15	1060	1097	10.7	13.6	14.6
2	15	1120	1098	10.3	13.9	*14.9
3	15	1180	1170	11.1	13.3	15.3
4	15	1190	1248	11.4	11.5	13.4
5	30	1940	1761		16.3	19.6
6	30	1860	1739		18.4	22.0
7	30	1820	1723		23.9	24.5
8	30	1920	1688		21.7	*22.2
9	45	2090	2039		19.7	*25.2
10	45	2270	2046		19.8	*26.2
11	45	2360	2092		18.8	*25.2
12	45	2230	2103		19.2	*24.6
13	60	2140	1947		15.5	16.4
14	60	2210	2021		16.3	17.9
15	60	2140	1933		14.8	18.5
16	60	2140	1961		14.3	17.6
17	75	1460	1430	10.2	7.3	12.8
18	75	1440	1450	9.8	7.3	12.6
19	75	1380	1283	9.6	13.4	14.4
20	75	1380	1316	9.4	13.5	14.2
21	90	1180	1270	6.1	5.5	6.7
22	90	1140	1260	5.7	5.0	6.1
23	90	1280	1280	5.7	4.2	5.7
24	90	1350	1349	5.7	4.8	6.7

*Significant strain reversal at failure.

TABLE V.- TEST RESULTS FOR HELICALLY AND CIRCUMFERENTIALLY WOUND TUBES

(a) International System of Units

Specimen	Nominal winding angle, α, deg	Shear modulus, $\bar{G}_{xy}$, MN/m^2		Experimental offset yield stress, $\bar{\tau}_y$, MN/m^2	$\bar{T}_{max}$, m-N	$\bar{\tau}_{max}$, MN/m^2
		Experimental	Analytical			
25	15, 90	9 600	9 350	60.0	2040	*136
26	15, 90	9 100	9 887	54.5	2080	*140
27	15, 90	9 000	9 584	60.7	2080	*141
28	15, 90	9 000	9 522	62.7	2060	*134
29	30, 90	11 900	11 377	104.1	2460	*174
30	30, 90	11 300	11 515	104.1	2350	*164
31	30, 90	11 200	11 439	111.0	2460	*173
32	30, 90	11 300	11 239	115.8	2430	*170
33	45, 90	13 400	12 880	159.3	2840	194
34	45, 90	13 200	12 728	157.2	2890	196
35	45, 90	13 800	13 445	157.9	2860	*194
36	45, 90	14 200	13 294	163.4	2870	200

(b) U.S. Customary Units

Specimen	Nominal winding angle, α, deg	Shear modulus, $\bar{G}_{xy}$, ksi		Experimental offset yield stress, $\bar{\tau}_y$, ksi	$\bar{T}_{max}$, in.-kips	$\bar{\tau}_{max}$, ksi
		Experimental	Analytical			
25	15, 90	1390	1356	8.7	18.1	*19.8
26	15, 90	1320	1434	7.9	18.4	*20.3
27	15, 90	1300	1390	8.8	18.4	*20.4
28	15, 90	1310	1381	9.1	18.2	*19.5
29	30, 90	1720	1650	15.1	21.8	*25.3
30	30, 90	1640	1670	15.1	20.8	*23.8
31	30, 90	1620	1659	16.1	21.8	*25.1
32	30, 90	1640	1630	16.8	21.5	*24.6
33	45, 90	1950	1868	23.1	25.1	28.1
34	45, 90	1920	1846	22.8	25.6	28.4
35	45, 90	2000	1950	22.9	25.3	*28.1
36	45, 90	2060	1928	23.7	25.4	29.0

*Significant strain reversal at failure.

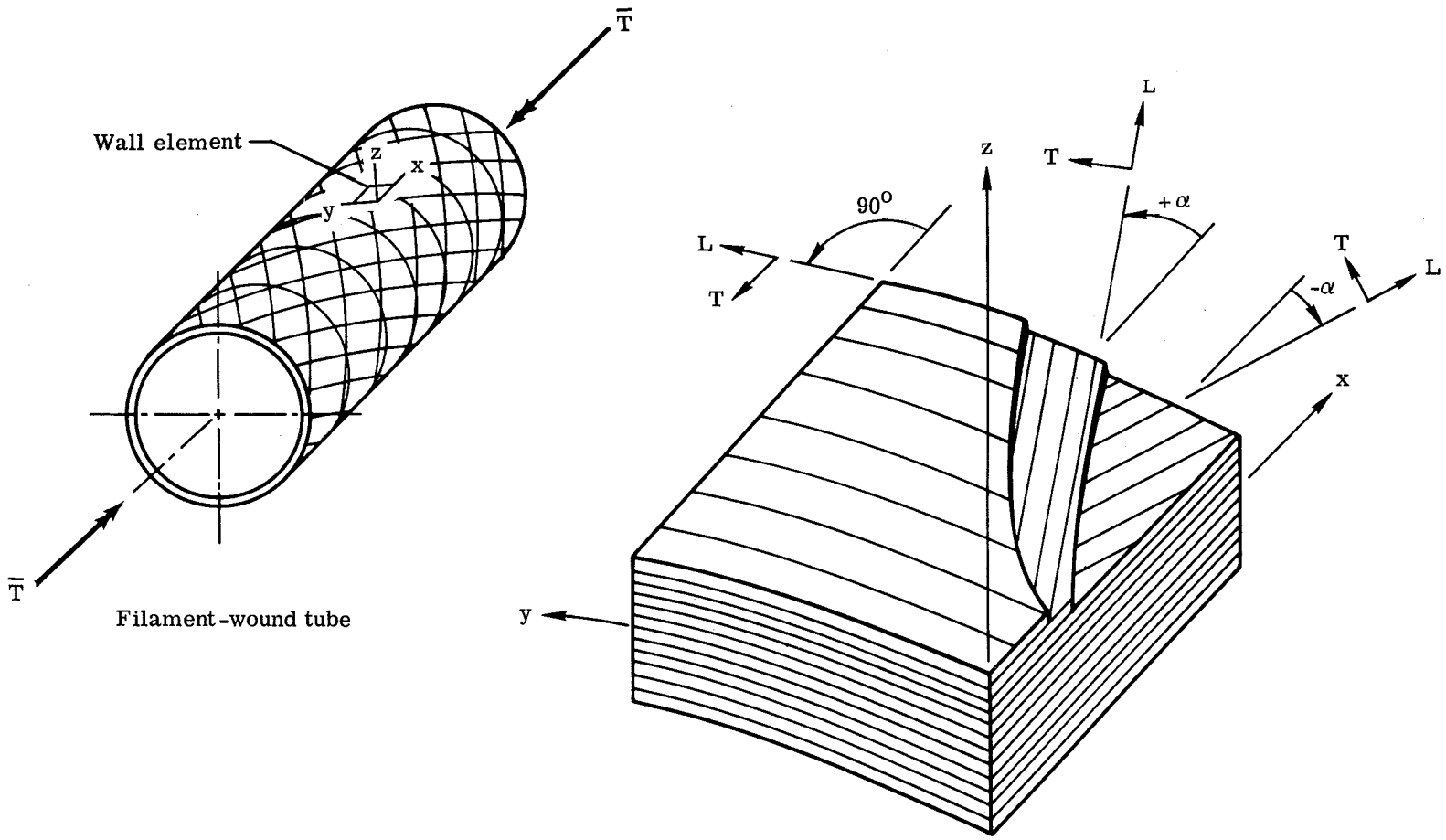

Figure 1.- Notation and coordinate systems for filament-wound tubes.

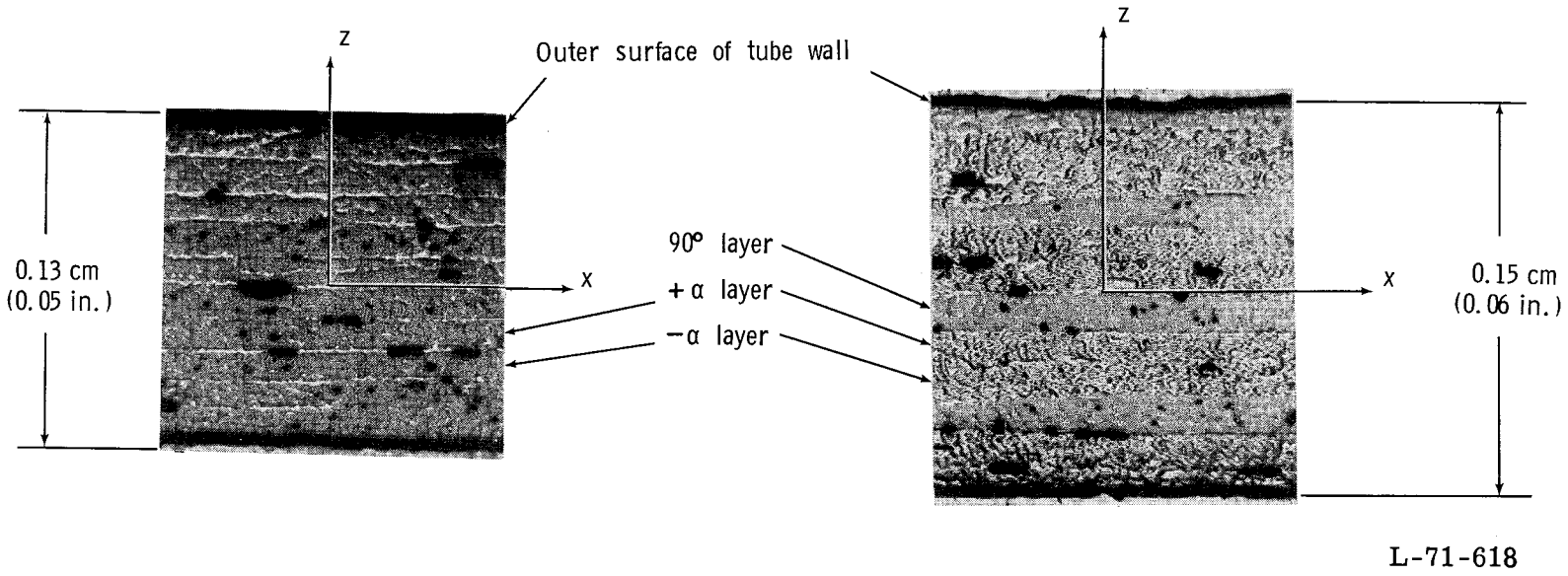

(a) Helically wound tube.

(b) Helically and circumferentially wound tube.

Figure 2.- Photomicrographs of sections through the walls of filament-wound tubes.

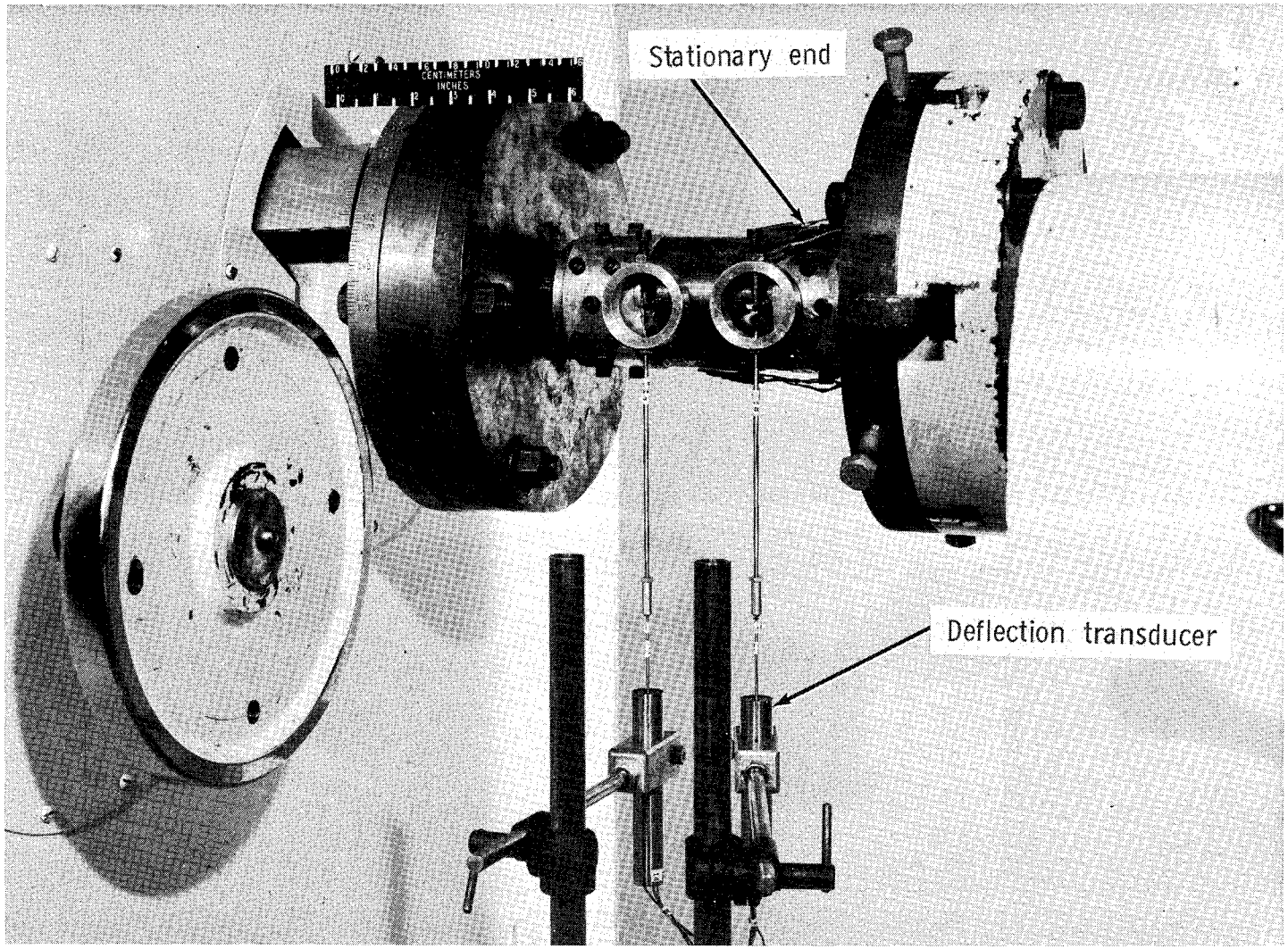

(a) Overall view prior to test. L-69-2940.1

Figure 3.- Torsion test setup.

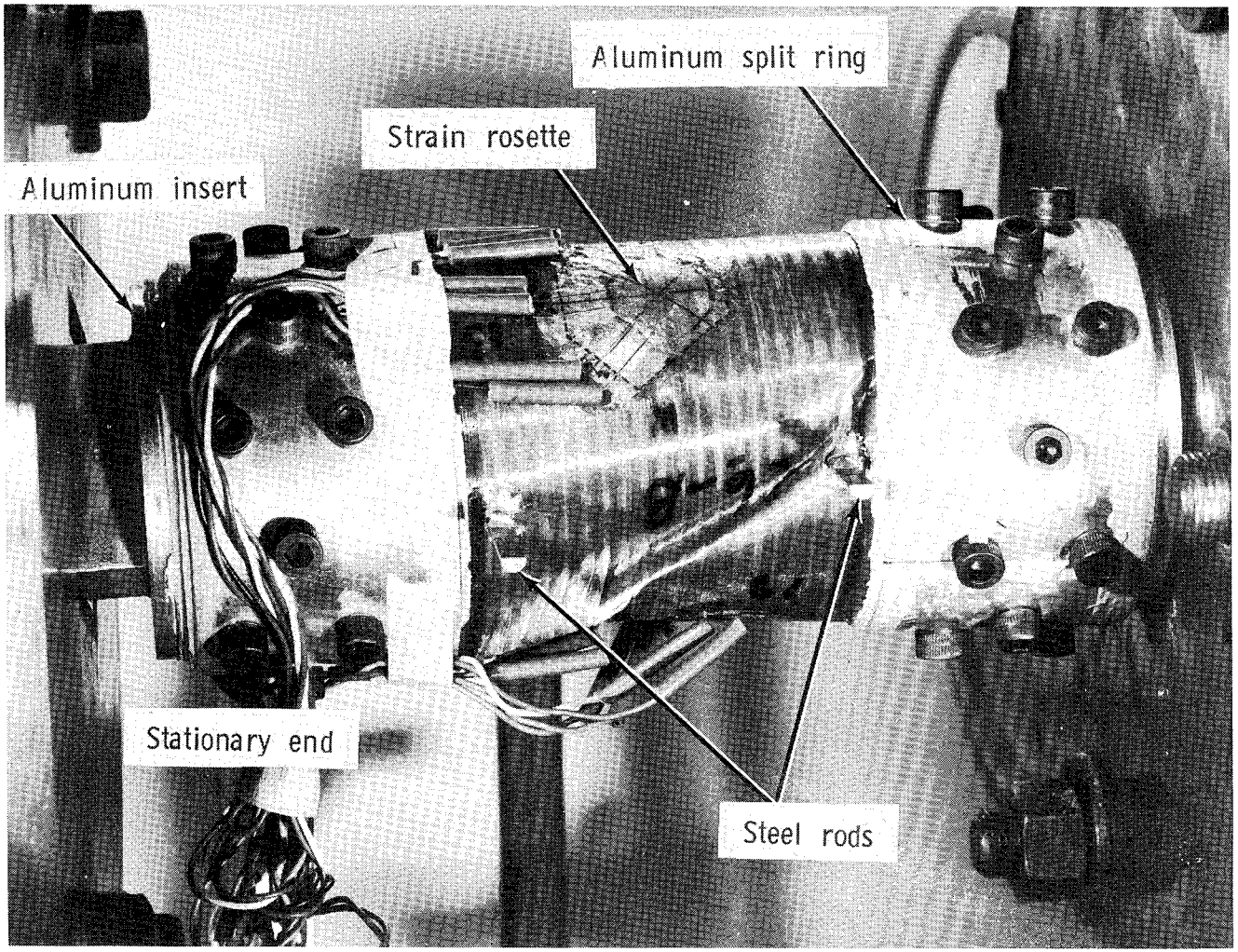

(b) Close-up showing failure of tube under loading. L-69-2326.1

Figure 3.- Concluded.

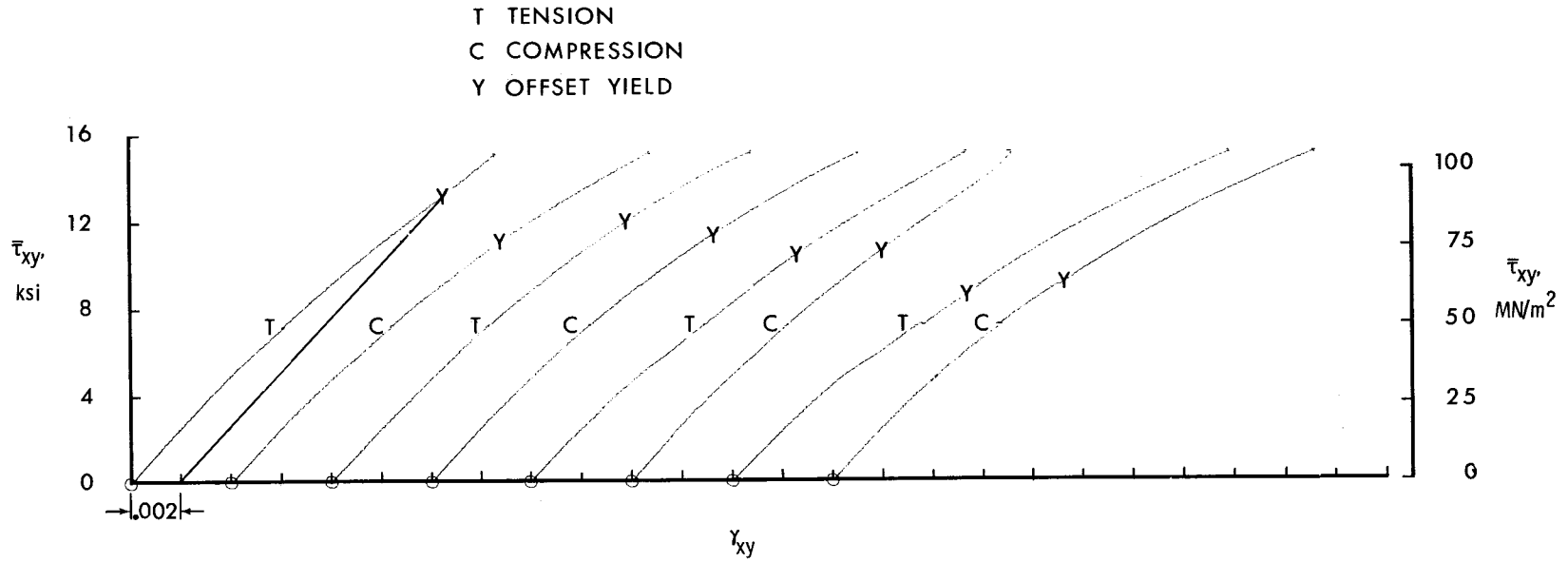

Figure 4.- Stress-strain behavior of specimen with yielding.

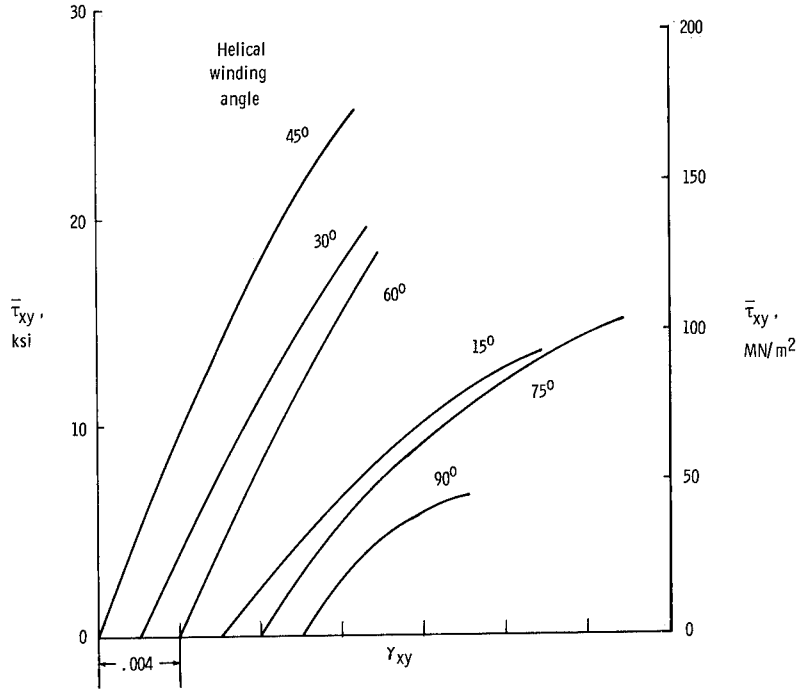

(a) Tubes with only helical windings.

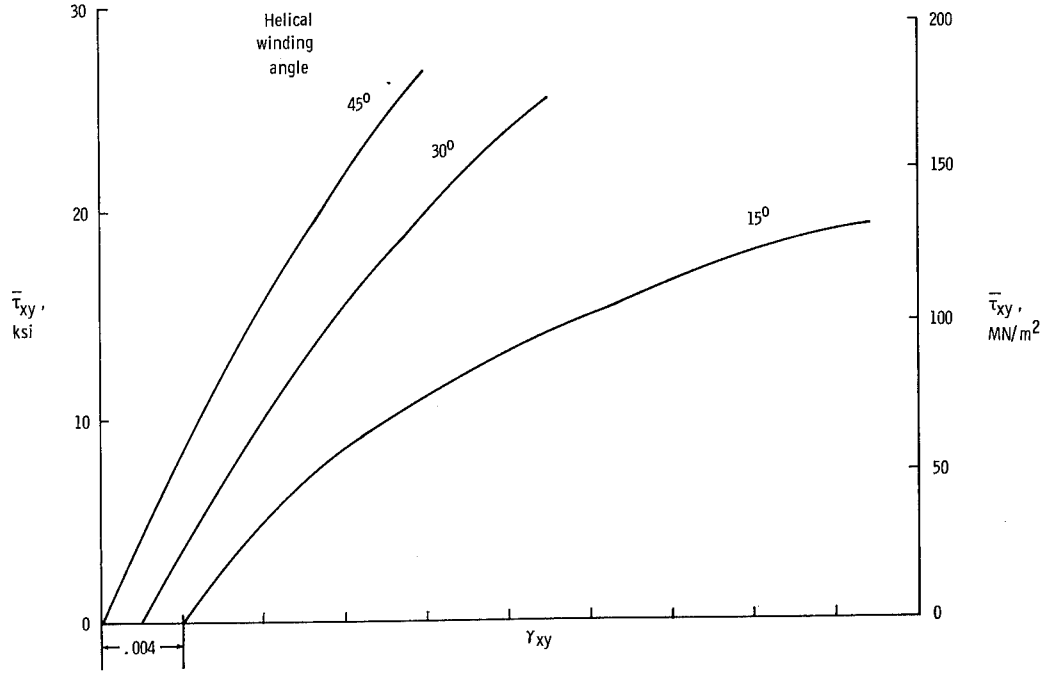

(b) Tubes with helical and circumferential windings.

Figure 5.- Typical shear stress-strain behavior for test specimens.

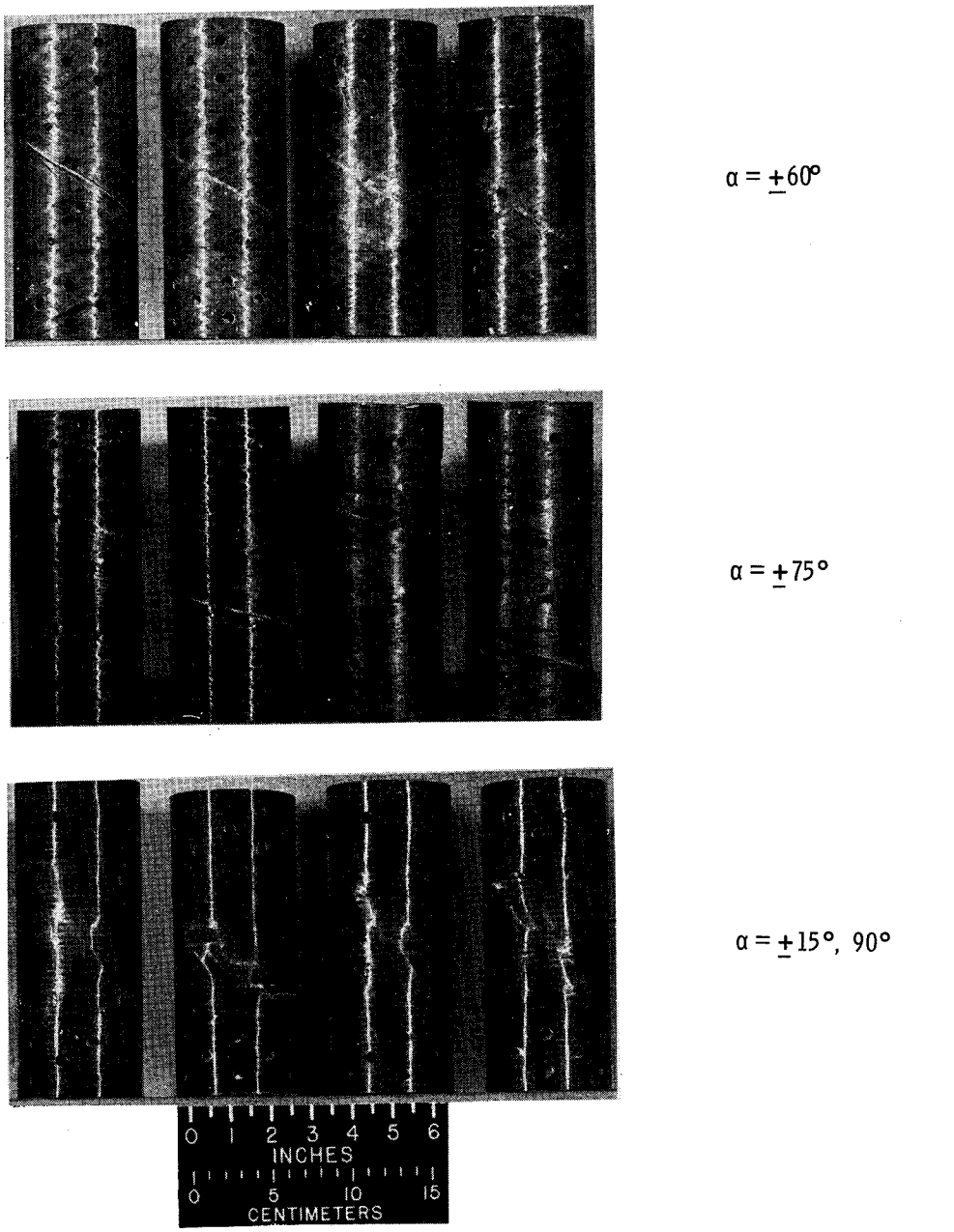

Figure 6.- Typical appearance of tubes at conclusion of torsion tests.

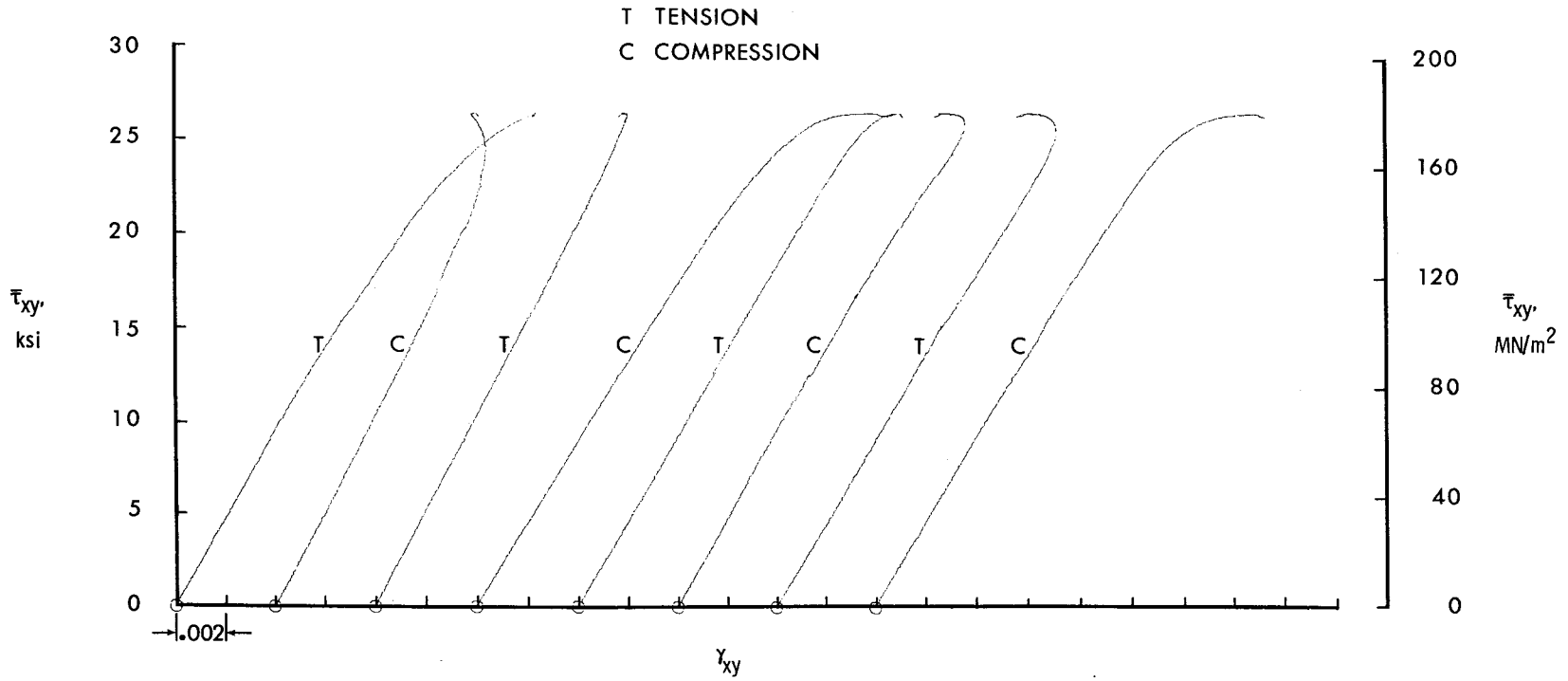

Figure 7.- Stress-strain curves for a specimen exhibiting strain reversal.

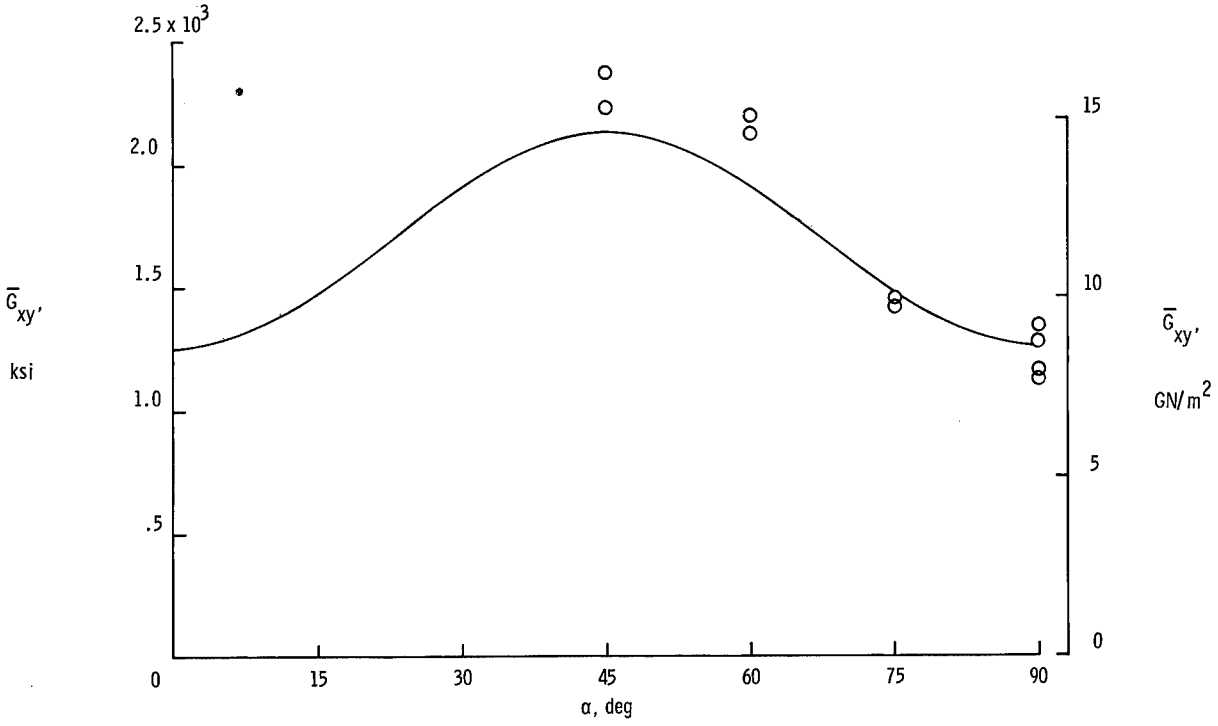

(a) Tubes with only helical windings.

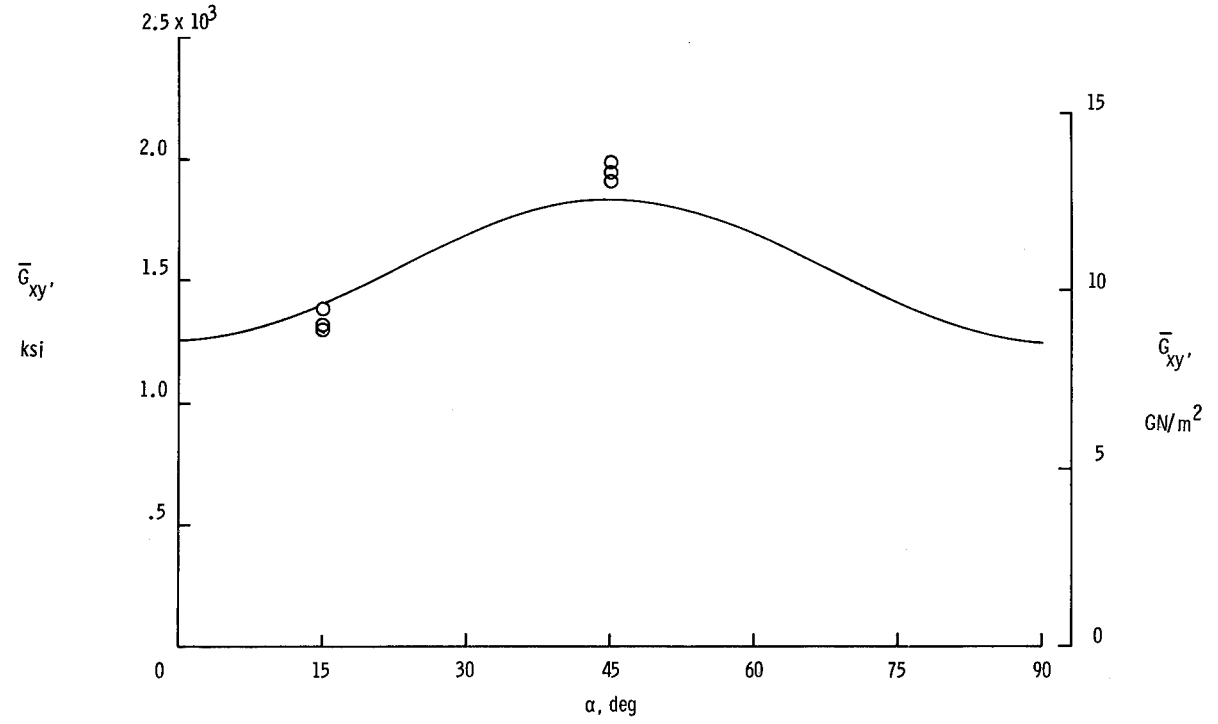

(b) Tubes with helical and circumferential windings.

Figure 8.- Comparison of computed effective shear modulus of tube wall with experimental results. $v_f = 0.63$; $\zeta_t = 3.0$; $\zeta_s = 3.5$.

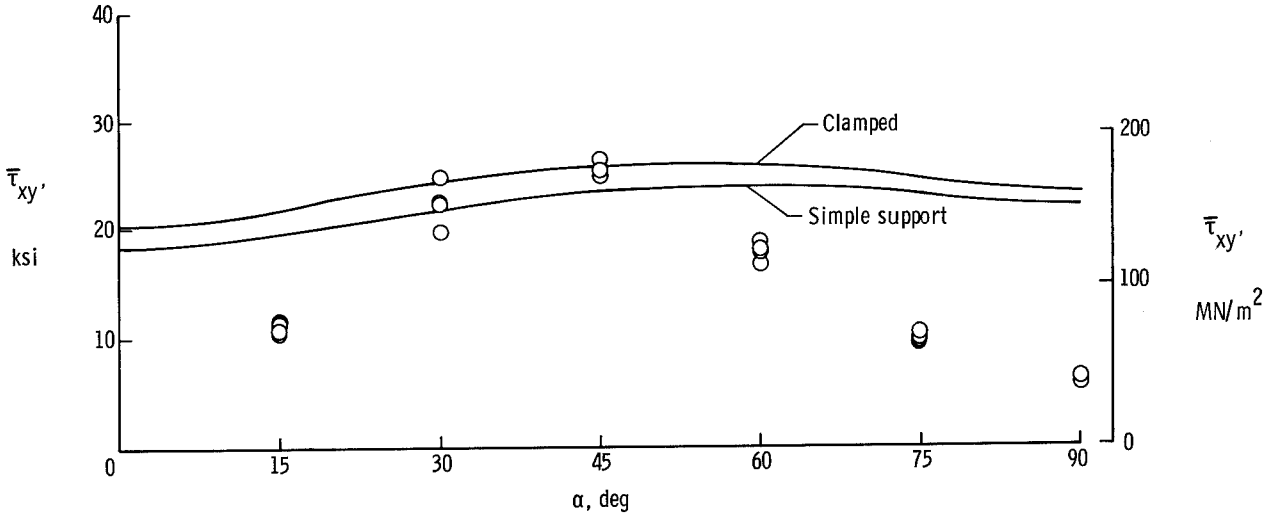

(a) Tubes with only helical windings. $t = 0.13$ cm (0.05 in.); $\frac{R}{t} = 30$.

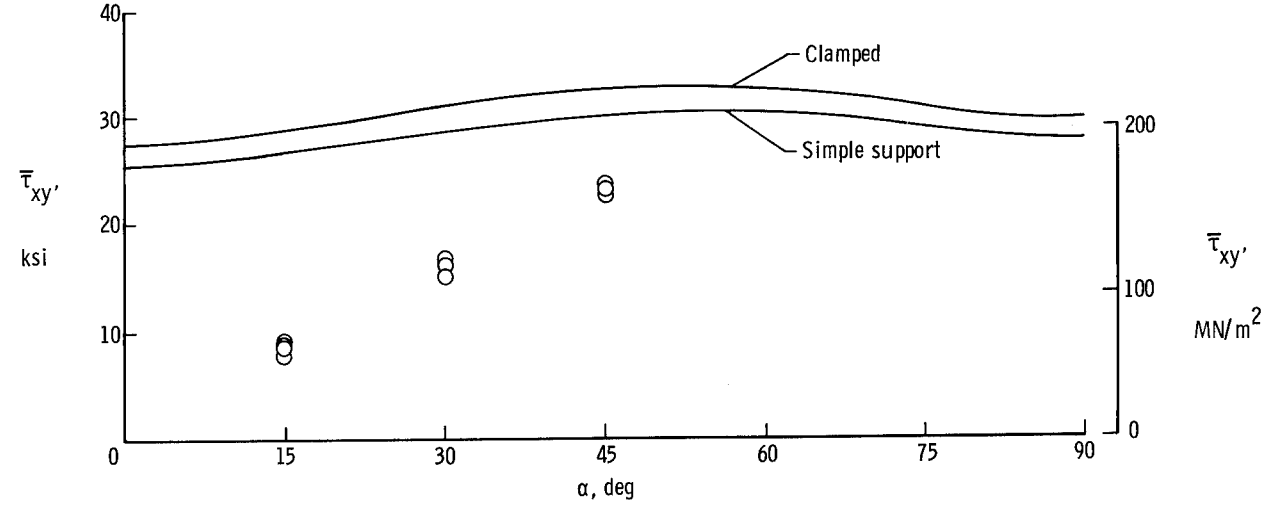

(b) Tubes with helical and circumferential windings. $t = 0.15$ cm (0.06 in.); $\frac{R}{t} = 25$.

Figure 9.- Comparison of experimental torsional strengths of tubes with torsional buckling predictions. $v_f = 0.63$; $\zeta_t = 3.0$; $\zeta_s = 3.5$; $\frac{l}{R} = 2$.

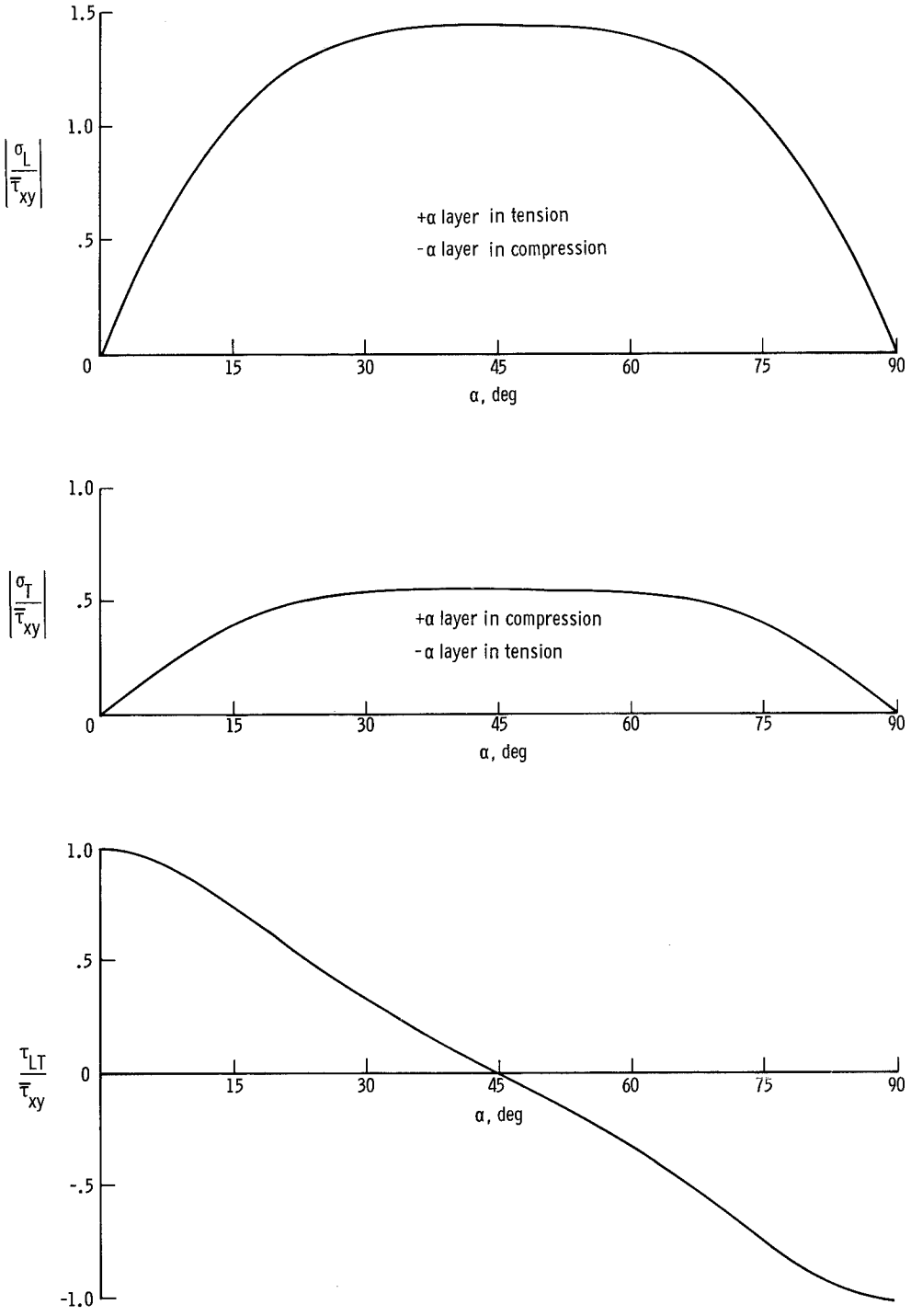

Figure 10.- Variation of stress with helical winding angle in tubes with only helical windings. $v_f = 0.63$; $\zeta_t = 3.0$; $\zeta_s = 3.5$.

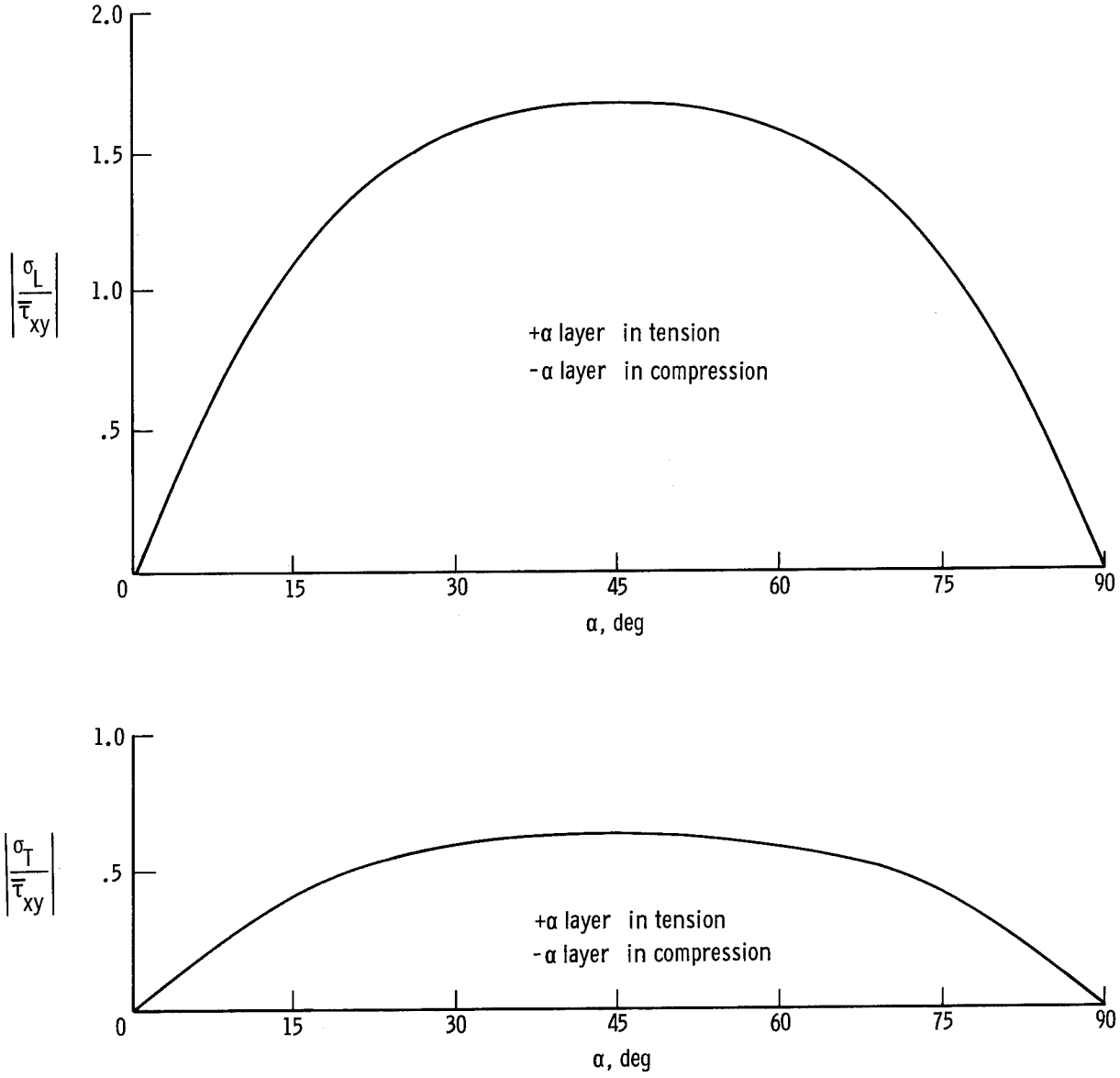

(a) Normal stresses in helically wound layers.

Figure 11.- Variation of stress with helical winding angle in tubes with helical and circumferential windings. $v_f = 0.63$; $\zeta_t = 3.0$; $\zeta_s = 3.5$.

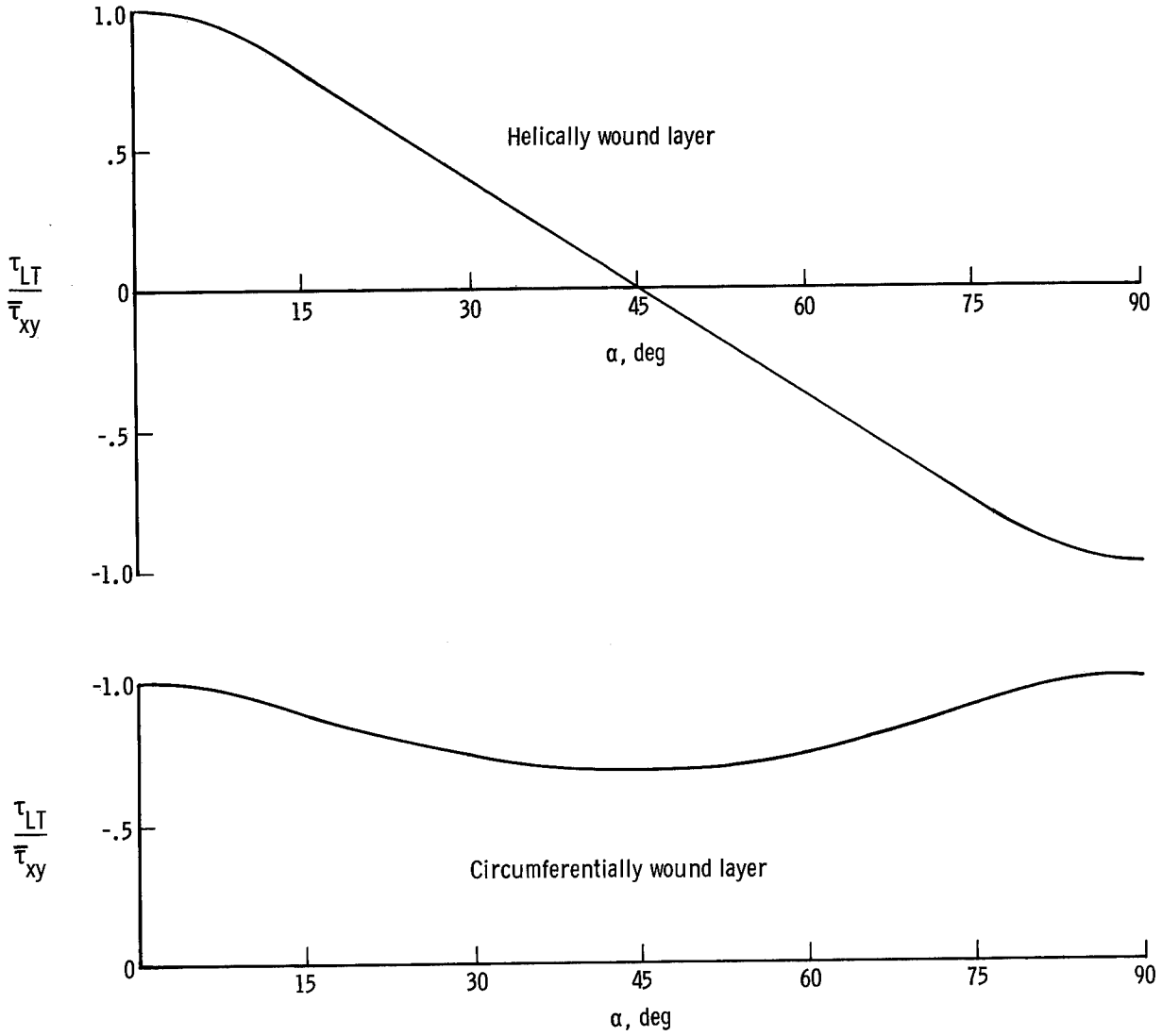

(b) Shear stress in helically and circumferentially wound layers.

Figure 11.- Concluded.

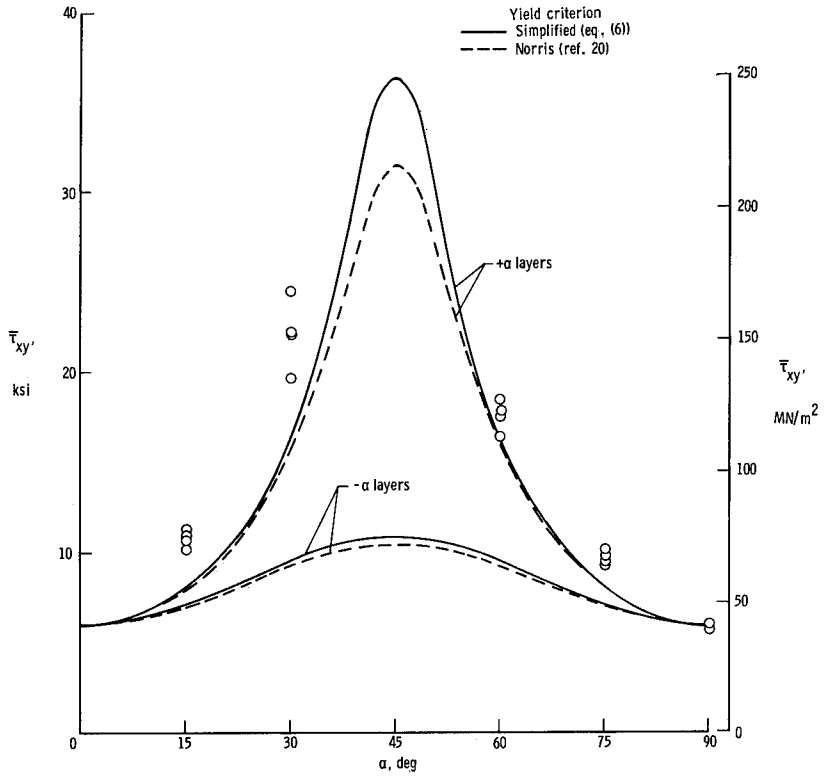

(a) Tubes with only helical windings.

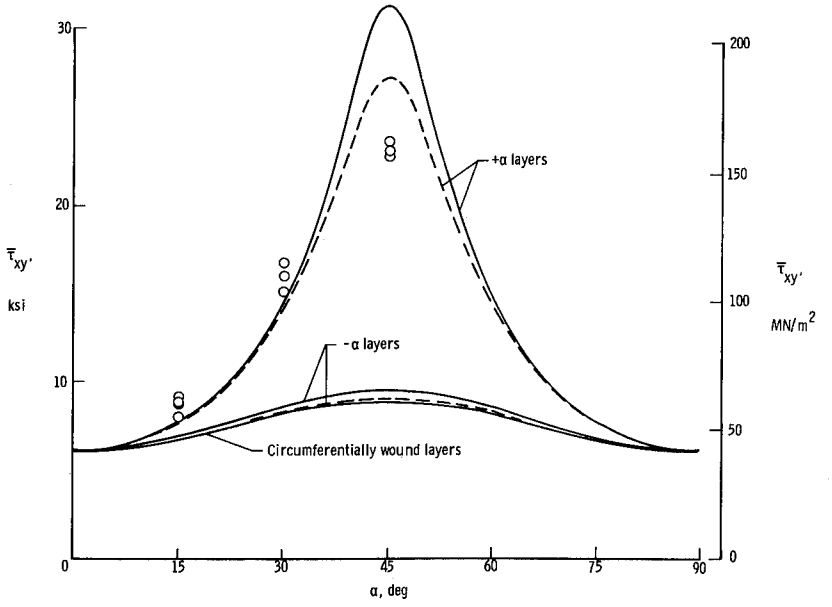

(b) Tubes with helical and circumferential windings.

Figure 12.- Comparison of experimental torsional strengths of tubes with analytical predictions based on orthotropic yield criteria. $v_f = 0.63$; $\zeta_t = 3.0$; $\zeta_s = 3.5$.

NASA-Langley, 1971 — 32 L-7058

"The aeronautical and space activities of the United States shall be conducted so as to contribute . . . to the expansion of human knowledge of phenomena in the atmosphere and space. The Administration shall provide for the widest practicable and appropriate dissemination of information concerning its activities and the results thereof."

—NATIONAL AERONAUTICS AND SPACE ACT OF 1958

NASA SCIENTIFIC AND TECHNICAL PUBLICATIONS

TECHNICAL REPORTS: Scientific and technical information considered important, complete, and a lasting contribution to existing knowledge.

TECHNICAL NOTES: Information less broad in scope but nevertheless of importance as a contribution to existing knowledge.

TECHNICAL MEMORANDUMS: Information receiving limited distribution because of preliminary data, security classification, or other reasons.

CONTRACTOR REPORTS: Scientific and technical information generated under a NASA contract or grant and considered an important contribution to existing knowledge.

TECHNICAL TRANSLATIONS: Information published in a foreign language considered to merit NASA distribution in English.

SPECIAL PUBLICATIONS: Information derived from or of value to NASA activities. Publications include conference proceedings, monographs, data compilations, handbooks, sourcebooks, and special bibliographies.

TECHNOLOGY UTILIZATION PUBLICATIONS: Information on technology used by NASA that may be of particular interest in commercial and other non-aerospace applications. Publications include Tech Briefs, Technology Utilization Reports and Technology Surveys.

Details on the availability of these publications may be obtained from:

SCIENTIFIC AND TECHNICAL INFORMATION OFFICE

NATIONAL AERONAUTICS AND SPACE ADMINISTRATION

Washington, D.C. 20546